Three-Dimensional Viscous Flow Computations Using the Integral Boundary Layer Equations Simultaneously Coupled with a Low Order Panel Method

by

William Michael Milewski

B.S., Webb Institute of Naval Architecture, 1986

Submitted to the Department of Ocean Engineering
in partial fulfillment of the requirements for the degree of

Doctor of Philosophy in Hydrodynamics

at the

MASSACHUSETTS INSTITUTE OF TECHNOLOGY

June 1997

Author .....
Department of Ocean Engineering
May 16, 1997

Certified by .....
Justin E. Kerwin
Professor of Naval Architecture
Thesis Supervisor

Accepted by .....
J. Kim Vandiver
Chairman, Departmental Committee on Graduate Students

Three-Dimensional Viscous Flow Computations Using the Integral Boundary Layer Equations Simultaneously Coupled with a Low Order Panel Method

by

William Michael Milewski

Submitted to the Department of Ocean Engineering
on May 16, 1997, in partial fulfillment of the
requirements for the degree of
Doctor of Philosophy in Hydrodynamics

Abstract

In this thesis a computational method for predicting the effects of viscosity on the global features of three-dimensional lifting surface flows such as lift, drag, and separation is presented. A simultaneous viscous/inviscid interaction algorithm is developed using a low order potential based panel method and the three-dimensional integral boundary layer equations. The viscous influence on the outer inviscid flow is modeled with source distributions superimposed on the lifting surface and potential flow wake. Equations for the boundary layer edge velocities, expressed as the sum of the inviscid edge velocity and a correction which depends only on the boundary layer variables, are developed from the panel method calculation. The boundary layer equations are discretized using finite elements and solved by a full Newton method. By introducing the influence of the potential flow solution into the Newton method Jacobian matrix, the global elliptic interaction of the inner and outer flows at separation is captured.

Numerical predictions are presented for a finite swept wing, an annular wing, and a two-dimensional hydrofoil section to validate the method. Predicted forces, pressure distributions, and boundary layer integral thicknesses are shown to be in good agreement with experimental data for flows with three-dimensional effects and separation.

Thesis Supervisor: Justin E. Kerwin
Title: Professor of Naval Architecture

Acknowledgments

Many people contributed to the research presented in this thesis. First, I thank my advisor Prof. Jake Kerwin for his support, encouragement, and willingness to listen to me babble, even about mass defect influence coefficients. I hope that some of his experience has rubbed off me and will make me a better engineer in the years to come. I would also like to thank the other members of my thesis committee for the many helpful suggestions they made along the way. Prof. Jerry Milgram presented me with the opportunity to work on this project and provided his keen engineering insight. Prof. Mark Drela became my personal expert in the boundary layer field and was seemingly on call 24 hours a day. Dr. David Greeley provided my pre-M.I.T. education in hydrodynamics and was kind enough to continue to advise me. The FEM utility subroutines used in my program were supplied by Dr. Brian Nishida.

As one of Prof. Kerwin's students I automatically became a member of the PropNuts. Special thanks go to all of the other members, especially Scott Black who entered and leaves M.I.T. with me. Early in my stay here I was an honorary member of the Acoustics Group as well. Matt Conti, Tarun Kapoor, and Joe Bondaryk kept me entertained with their banter and craziness. Finally, I thank the friends I've shared an office with over the last 5 years: Hiren Maniar, Bill Ramsey, Lt. Cmdr Greg Thomas, John Mass, and Nicole Suoja.

Rich Kimball and Lt. Cmdr Alex Desroches were kind enough to review my thesis as I struggled to complete it. Their suggestions and encouragement help me finish when I didn't think it was possible.

This thesis is dedicated to my wife Maura who stood by me while I selfishly pursued my education.

My studies at M.I.T. were funded in part by the Office of Naval Research Graduate Fellowship Program and the *America*^{3} Foundation.

Contents

List of Tables

Chapter 1

Introduction

Inviscid-flow calculation techniques, such as panel methods, are well-developed and routinely used in the design and analysis of ships and their components. While these methods are robust and can provide reasonable answers quickly, they are incapable of predicting viscous effects such as separation. Viscous three-dimensional flows are presently computed with Navier-Stokes solvers. Although the numerical solution of the Navier-Stokes equations has become more practical in recent years, it still requires considerable computational effort. Viscous flows can be computed more efficiently using viscous/inviscid interaction (VII) methods. These methods are less general than Navier-Stokes solvers and can fail in some separated flows, yet have been used with as much success as Navier-Stokes solvers by the aeronautical research community.

A computational method based on VII is presented here to analyze three-dimensional lifting surface flows with separation. Whereas existing VII methods have been developed specifically for compressible flows which preclude the use of panel methods, the current method is designed for hydrodynamic flows. The model couples a low order panel method with the three-dimensional integral boundary-layer equations using a ully simultaneous coupling scheme.

1.1 Viscous/Inviscid Interaction

Prandtl's boundary-layer concept provides the important link between a real fluid and an ideal fluid. In high Reynolds number external flows, viscous effects are confined to thin boundary layers which form along the body. Outside of these regions the flow is essentially inviscid and irrotational. With the assumption that the boundary layer is thin compared to the characteristic body length, Prandtl showed that the pressure

can be assumed constant through the boundary layer and diffusion neglected, except in the direction normal to the wall. When these simplifications are applied to the Navier-Stokes equations, the first order boundary-layer equations are obtained.

VII methods separate the flow field into distinct viscous and inviscid regions. Individual calculations are made for the two regions and combined with a coupling scheme to obtain a composite solution. Because each part of the flow field is represented with a simplified model, the overall computational cost is less than solving the complete problem directly.

Efficient solutions to the outer inviscid flow in hydrodynamic applications can be computed using boundary integral element (panel) methods [21, 36] because the region is incompressible and irrotational. Not only do panel methods reduce the size of the numerical problem, but they eliminate such issues as three-dimensional gridding of the flowfield and farfield boundary conditions altogether. Solutions for the viscous region are approximated using the boundary-layer equations. The inviscid and viscous flows are coupled through the boundary conditions for each problem. The inviscid flow provides the pressure field that is impressed upon the boundary layer while the boundary-layer solution displaces the outer flow away from the body.

1.2 Research History

Three-dimensional boundary-layer methods have been used previously to analyze flow over marine propellers and ship hulls. However, none of the methods included interaction with the outer inviscid flow. Groves [13] developed a prediction method for propeller blades using the integral boundary-layer equations. Groves and Chang [14] and Oshima [42] presented methods based on the differential equations for the analysis of the boundary layers on propeller blades. The feature common to all of these methods is that the outer flow edge velocities are not updated. After the completion of one sweep, or if separation is encountered, the boundary-layer calculations stop.

In interacting boundary-layer calculations, a transpiration boundary condition on the body surface provides the coupling mechanism for the inviscid and viscous regions. The boundary condition is implemented by applying a source distribution along the body in the inviscid model, simulating the displacement effect of the boundary layer. Source strengths are set by the rate of growth of the boundary layer. The solutions

to the inner and outer problems are recomputed, and the source strengths updated, until the normal and tangential velocity components for the potential flow and the boundary layer are equal. The procedure which is used to combine the individual solutions is known as the coupling algorithm.

The coupling algorithms which have been used in two dimensions include direct, inverse, semi-inverse, quasi-simultaneous, and simultaneous coupling. The first three are examples of weak coupling schemes that combine the solutions to the viscous and inviscid regions of the flow iteratively. Quasi-simultaneous and simultaneous coupling solve the two regions of the flow together, making them more reliable for flows with strong interaction. Additional information on the various schemes, as well as references for two-dimensional VII applications, is presented in the review paper by Lock and Williams [33]. More recent references to two-dimensional calculations are given in [1].

Weak coupling methods are typically used for three-dimensional interacted flows. In a direct scheme, the outer flow is computed with the transpiration source strengths prescribed, followed by the solution of the boundary-layer equations with the edge velocities prescribed. The iteration cycle is repeated until the solution converges. The direct method converges for attached flows, but fails when the wall shear stress vanishes in 2-D and at separation lines in 3-D. Coney [5] calculated propeller blade flows using a 2-D strip integral boundary-layer solver directly coupled with a three-dimensional panel method. Full three-dimensional methods using direct coupling have been developed by Lazareff and Le Balleur [30] for predicting transonic flow over finite wings.

Separated flows can be calculated by solving the boundary-layer equations in inverse mode with the displacement thickness or skin friction prescribed [3]. Three-dimensional VII methods based on the inverse boundary layer equations generally use semi-inverse coupling to avoid convergence problems encountered with full inverse coupling [33]. The semi-inverse procedure uses a direct calculation of the inviscid flow and an inverse calculation of the viscous flow to provide two estimates of the edge velocities. The edge velocities are combined in a correction formula that provides the source strengths for the transpiration boundary conditions. Each flow is recomputed until the edge velocities agree. Methods based on this approach have been developed by Wigton and Yoshihara [56] and Kovalev [27] for transonic flows. The

scheme should converge for separated flows, but Wai and Yoshihara [53] encountered numerical problems for wing calculations with trailing edge separation.

The fully simultaneous coupling scheme has proved to be the most robust for two-dimensional separated flows. This scheme solves the inner and outer flows simultaneously, rather than iteratively, to determine the transpiration source strength and edge velocity.

Two simultaneous coupling algorithms have been presented by Drela for two-dimensional flows. The first combines the integral boundary-layer equations with the Euler equations [9]. The second method couples the integral boundary-layer equations with a linear-vorticity streamfunction panel method [10] and was introduced to improve the speed of the algorithm.

Hufford [20] replaced the panel method in Drela's algorithm with a low order perturbation potential panel method. The procedure was subsequently extended to permit coupling of the two-dimensional boundary-layer method with a three-dimensional panel method and used to analyze viscous flow over propeller blades along constant radius strips. The method is stable in separated flows, but requires an assumption about the marching direction and is invalid for boundary layers with significant cross-flow.

Nishida [41] recently developed a VII method to analyze three-dimensional compressible flow over wing geometries with separation. The outer flow is modeled using the full potential equation and the viscous flow is modeled using the three-dimensional integral boundary layer equations. Equations for the edge velocities are derived from a wall transpiration condition. The full potential equation is solved on a 3-D grid in the flow field surrounding the wing to permit prediction of transonic flows. Fully simultaneous coupling is implemented by solving the full potential, boundary-layer, and edge velocity equations together by Newton's method. Nishida's method is conceptually similar to the one developed here, however, the implementation of the coupling procedure and associated strengths and weaknesses of the two methods are significantly different. Some of the differences include: the method of discretization, the representation of edge velocities, and the size and properties of the system of equations that is solved.

1.3 Overview of Method

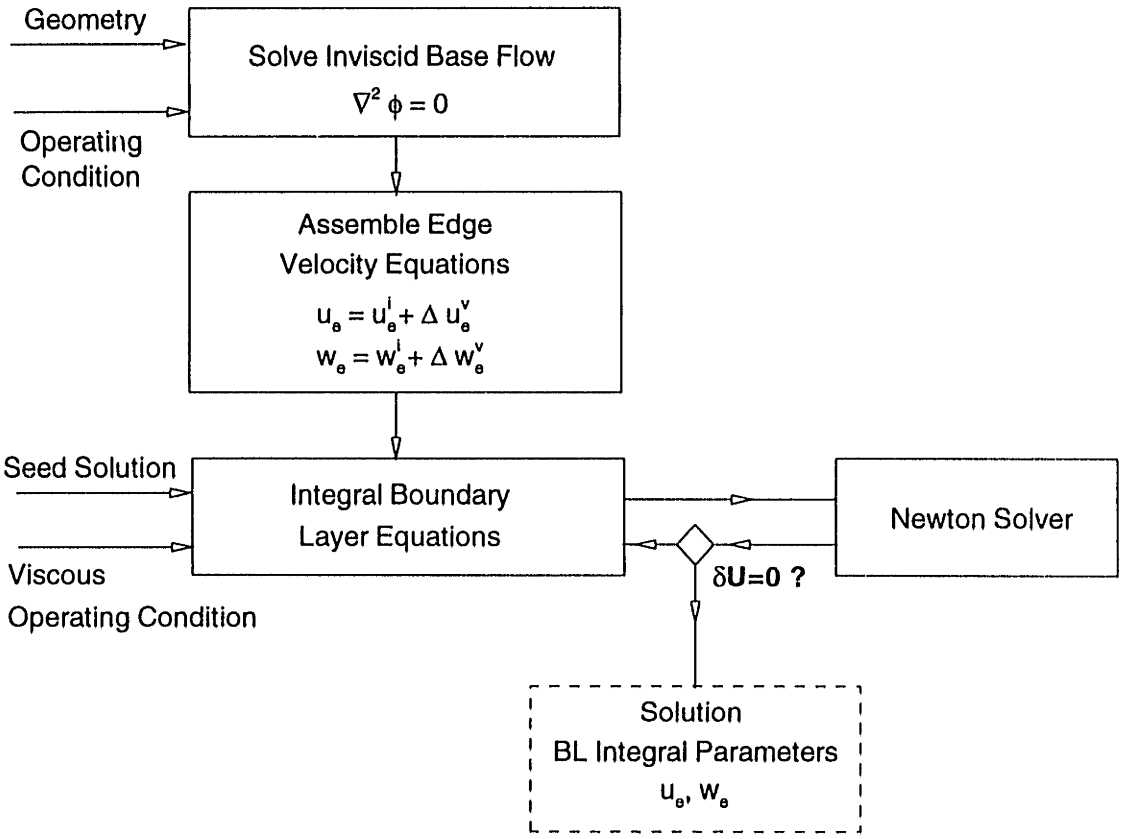

Figure 1-1: Flow Diagram for VII Solver

An overview of the simultaneous coupling algorithm described in this thesis is presented in Figure 1-1. First, the outer flow is solved by a low order panel method with a set of initially unknown transpiration sources. The calculation requires a description of the body and wake surfaces and definition of the operating condition as input parameters, and supplies the inviscid edge velocities as an output. The edge velocity in the VII calculation is equal to the inviscid edge velocity plus a correction due to the displacement effect of the boundary layer. Equations relating the edge velocity to the boundary-layer variables are developed from the transpiration source influence coefficients. Finally, the three-dimensional integral boundary-layer equations are solved by Newton's method, with the edge velocity equations supplying the outer boundary conditions. By introducing the edge velocity equations, the system of boundary layer equations is made elliptic. An initial guess at the boundary-layer solution is required

and provided by a 2-D strip solution or a previous 3-D solution. The location of the laminar-to-turbulent transition line and the Reynolds number are also required as input parameters. The solution to the boundary-layer problem provides the integral thicknesses and the viscous edge velocities.

The computational procedure is intended to be a design tool that is capable of predicting the overall features of three-dimensional viscous flows including lift, drag, and separation. In part, this requires an accurate and efficient means of modeling the body and wake geometries. They are represented parametrically by tensor product B-splines surfaces here, making the geometric modeling compatible with existing computer aided design (CAD) packages. Furthermore, the edge velocity equations are constructed by numerically evaluating the surface gradient of the potential in B-spline parametric space. The grid metrics are calculated analytically using the B-spline expansion.

The method presented here may be used to predict the three-dimensional, incompressible, viscous flow over wings, hydrofoils, and annular wings and can be extended to predict flow over marine propeller blades. Some of the current limitations of the method are: it is incapable of predicting flow over non-lifting bodies with open separation, secondary flows at wing tips and wing/body junctions are not yet modeled, and only linearized wake geometries are assumed at this time.

Chapter 2

Inviscid Flow

The flow outside the boundary layer is modeled as an incompressible, potential flow. This chapter presents a boundary integral equation for the perturbation potential without considering the displacement effect of the boundary layer. A discrete form of the boundary integral equation is developed using a low order panel method.

2.1 Formulation of the Integral Equation

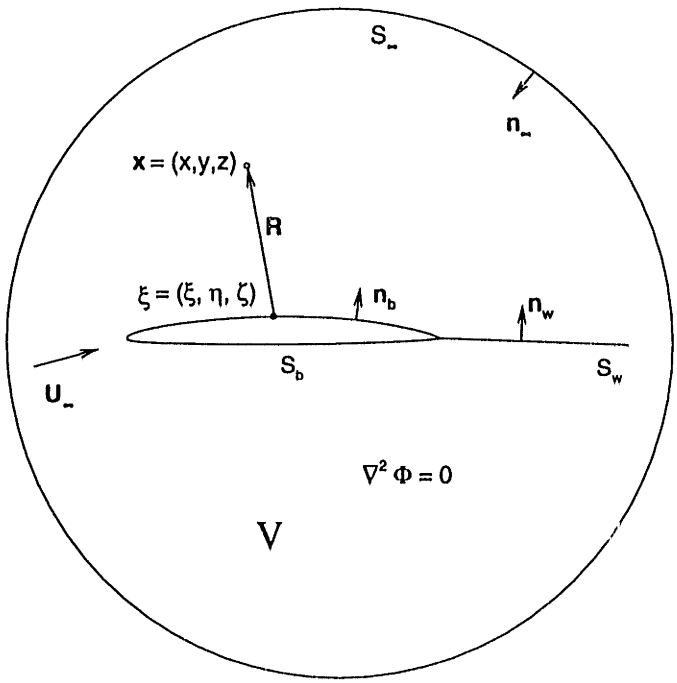

Figure 2-1: Section of the Potential Flow Domain for a 3-D Lifting Surface and Wake

Consider a three-dimensional lifting body immersed in an unbounded fluid and subject to an inflow velocity $\mathbf{U}_\infty$, as shown in Figure 2-1. The body is defined by the surface

$\mathbf{S}_b$ with a unit normal vector $\mathbf{n}_b$ pointing into the fluid volume $\mathbf{V}$. $\mathbf{V}$ is enclosed by the surface $\mathbf{S}_\infty$, with unit normal vector $\mathbf{n}_\infty$ also pointing into the volume.

The fluid inside $\mathbf{V}$ is assumed to be inviscid and incompressible. Furthermore, it is assumed to be irrotational, except possibly for a thin wake $\mathbf{S}_w$ which is shed from the trailing edge of the body. With these assumptions, the velocity may be defined as the gradient of a scalar potential Φ.

$$\mathbf{U} = \nabla\Phi \tag{2.1}$$

Substituting (2.1) into the continuity equation gives Laplace's equation which is the governing equation for an incompressible potential flow.

$$\nabla^2\Phi = 0 \tag{2.2}$$

The potential Φ may be decomposed into a component due to the free stream, ϕ_∞, and a perturbation potential, ϕ, due to the body.

$$\Phi = \phi_\infty + \phi \tag{2.3}$$

With ϕ_∞ given, Laplace's equation can be recast as an integral equation for the perturbation potential by applying Green's third identity.

$$4\pi T\phi(\mathbf{x}) = \iint_{\mathbf{S}_b} (\phi(\xi)\mathbf{n}_\xi \cdot \nabla G(\mathbf{x};\xi) - G(\mathbf{x};\xi)\mathbf{n}_\xi \cdot \nabla\phi(\xi))d\xi + \iint_{\mathbf{S}_w} \Delta\phi(\xi)\mathbf{n}_\xi \cdot \nabla G(\mathbf{x};\xi)d\xi \tag{2.4}$$

where the Greens function, G, and the velocity potential, ϕ, are solutions of the Laplace equation and T = 0, 1/2, or 1 for points outside, on the boundary, or inside $\mathbf{V}$. G is the Greens function for an unbounded fluid

$$G(\mathbf{x};\xi) = \frac{1}{R(\mathbf{x};\xi)} = \frac{1}{\sqrt{((x-\xi)^2 + (y-\eta)^2 + (z-\zeta)^2)}} \tag{2.5}$$

where $\mathbf{x}$ is a fixed point which may be located anywhere in space and ξ is the variable point in the integration.

The first integral on the right hand side of (2.4) is the induced potential at point $\mathbf{x}$ due to a continuous source distribution of strength $\mathbf{n}_b \cdot \nabla\phi$ and a continuous dipole distribution of strength ϕ on the body surface. The second integral is the induced potential at point $\mathbf{x}$ due to a continuous dipole distribution over the inviscid wake sheet $\mathbf{S}_w$ with a strength equal to the jump in potential across it.

$$\Delta\phi = \phi^u - \phi^l \tag{2.6}$$

The details of this derivation may be found in [29] and [40] for non-lifting bodies and [31], [17], and [36] for lifting bodies.

2.1.1 Boundary Conditions

Equation (2.4) defines a boundary value problem for the perturbation potential. Boundary conditions are required on all surfaces enclosing V to determine a unique solution.

Body Conditions

The body is initially assumed to be impermeable. The kinematic boundary condition requires that the normal components of the fluid and body velocities be equal at a point on the surface.

$$\mathbf{n}_b \cdot \nabla\phi = -\mathbf{U}_\infty \cdot \mathbf{n}_b \tag{2.7}$$

Outer Surface Conditions

The perturbation velocity due to the body should vanish on the outer control surface, $\mathbf{S}_\infty$, in the limit that the surface is an infinite distance from the body.

$$\nabla\phi \to 0, \qquad \text{as} \qquad \mathbf{S}_\infty \to \infty \tag{2.8}$$

Wake Conditions

The wake surface represents a surface of discontinuity in a three-dimensional lifting flow that must be excluded from the fluid volume because it contains the vorticity shed by the body. By applying conservation of mass and momentum to the interface, we can show that $\mathbf{S}_w$ is a force-free, material surface [36]. The pressure jump and jump in normal velocity are zero across the interface.

$$\begin{aligned} \Delta p &= 0 \\ \Delta(\mathbf{n}_w \cdot \nabla\phi) &= 0 \end{aligned} \tag{2.9}$$

A Kutta condition is required to uniquely specify the circulation that will make the flow velocity finite at the trailing edge.

$$|\nabla\phi|_{t.e.} < \infty \tag{2.10}$$

The shed vorticity is convected away from the trailing edge along S_w. This implies that the potential jump across the wake is constant along streamlines for a steady flow and equal to the jump in potential across the trailing edge of the lifting surface.

$$\Delta\phi_w = \Delta\phi_{te} \tag{2.11}$$

For a steady flow, the potential jump across the wake is the same as the circulation around the body.

2.2 Numerical Solution by Panel Method

This section presents a numerical method to calculate the inviscid flow without including the effects of the boundary layer. A solution to the coupled outer flow problem is obtained by combining this inviscid solution with a perturbation term due to the boundary layer, and is addressed in chapter 4.

2.2.1 Representation of the Body and Wake Geometries

The discrete boundary integral equation is solved on the "exact" body surface in our panel-method calculations; however, the wake geometry is linearized. Calculation of a force-free wake geometry, including roll-up of the free edge of the vortex sheet, can be treated using panel methods [44] [46], but requires significant computational effort and is beyond the scope of this thesis.

The wake is approximated as a flat sheet for wing calculations and a constant radius tube for circular duct calculations. It is assumed to follow the nose-tail line of the airfoil section, extending several chord lengths downstream of the body trailing edge where it is truncated.

The body and wake surfaces are represented parametrically using tensor product B-spline expansions of the form

$$\mathbf{X}(s,t) = \sum_{i=1}^{\bar{N}_s} \sum_{j=1}^{\bar{N}_t} \mathcal{X}_{i,j} S^{i,j}(s,t) \tag{2.12}$$

where $\mathbf{X}(s,t)$ is a point on the surface, $\mathcal{X}_{i,j}$ are known control net vertices, $S^{i,j}(s,t)$ are the rational surface B-spline basis functions in the parametric variables s and t. $\bar{N}_s$ and $\bar{N}_t$ are the number of vertices in s and t directions respectively. Each surface spline is referred to as a patch.

The coordinates of the control net vertices can be calculated by surface interpolation or constructed by a geometric modeling package. The geometries analyzed in this research were topologically simple and could be formed by stacking spanwise two-dimensional B-spline polygons that were calculated using a fitting routine developed by Kerwin [23]. The vertices are specified in the body-fixed, $\mathbf{X}_o$, coordinate system.

Figure 2-2 shows the body-fixed and parametric coordinates for a section of a wing. The origin of the chordwise spline is at the trailing edge on the lower surface of the wing. Note that s and t do not necessarily define directions which are orthogonal in physical space.

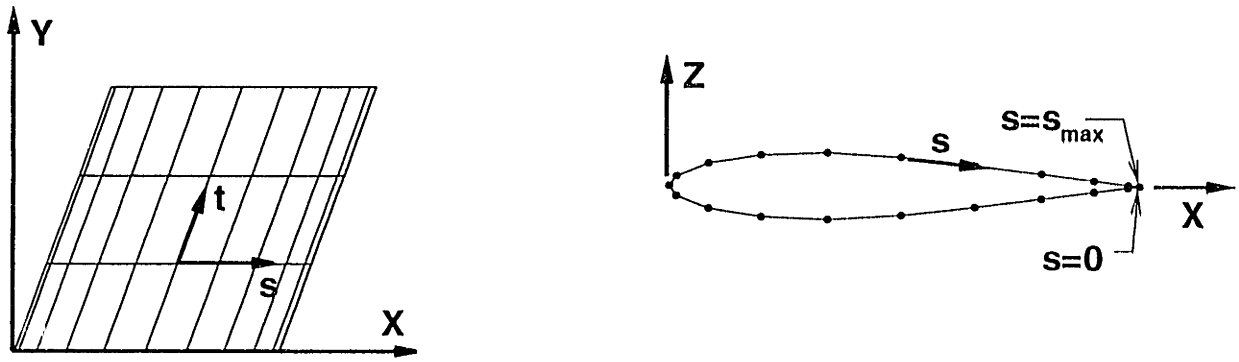

Figure 2-2: Body-fixed and parametric coordinate systems for a section of a 3-D wing. The grid lines are evaluated along s=*const* and t=*const*

A local orthogonal, curvilinear coordinate system, x, is constructed on each body and wake surface using the B-spline expansion as described in Appendix A. On body patches, the origin is located at the junction of the image plane and trailing edge on the lower surface of the airfoil section. The x coordinate, which is taken tangent to chordwise grid lines, wraps around the airfoil section contour, ending at the trailing edge on the upper surface. The remaining coordinates are given by the local outward normal, y, and second surface tangent vector, z. The surface coordinate system is shown in Figure 2-3.

2.2.2 Discrete Integral Equation

A discrete representation of the boundary value problem is obtained by applying a low order panel method to the integral equation (2.4). The panel method is a technique for solving boundary integral equations where the body and wake surfaces

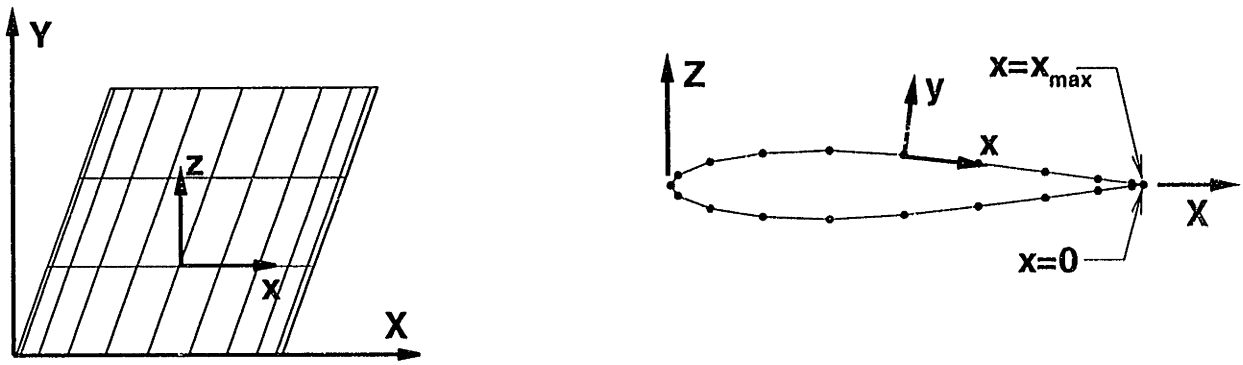

Figure 2-3: Body-fixed and local surface coordinate systems for a section of a 3-D wing. The body-fixed coordinates are denoted by (X,Y,Z) and the local surface coordinates by (x,y,z).

are described by a finite number of flat, quadrilateral panels (see Figure 2-4), and the integral equation is enforced at a similar number of collocation points. The surface integrals are replaced by a summation of integrals over the individual panels. In a low order scheme, the singularity distribution is assumed to be uniform over each panel, therefore ϕ and $\frac{\partial \phi}{\partial n}$ may be moved outside of the integrals and set equal to the value at the collocation point, taken at the panel centroid in our method. The source strength of the j^{th} panel, $(\frac{\partial \phi}{\partial n})_j$, is set by enforcing the kinematic boundary condition (2.7) at the collocation point.

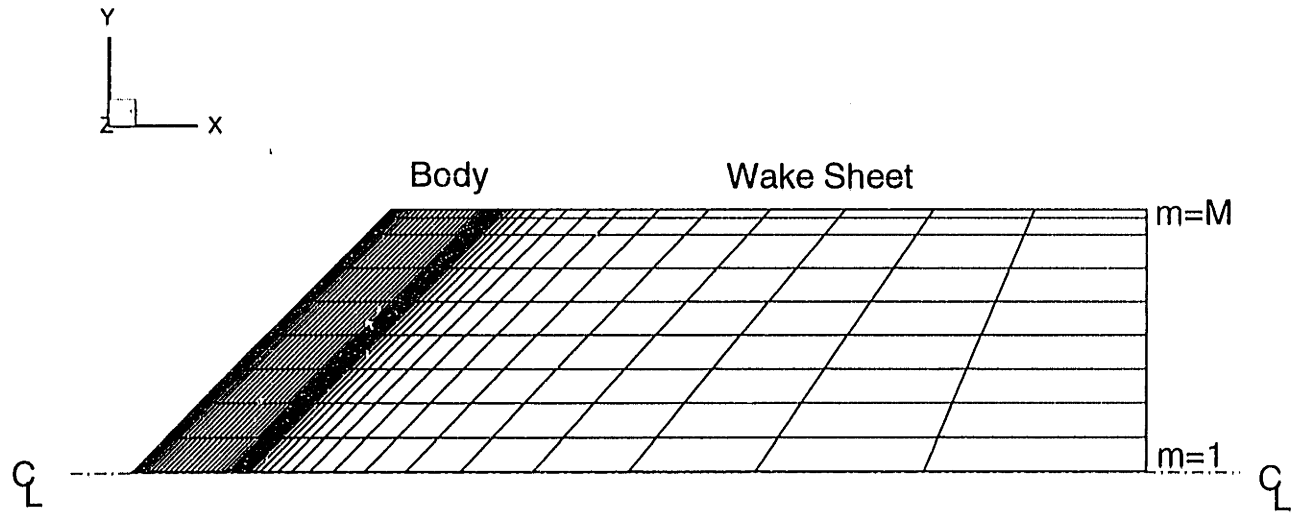

Figure 2-4: Discretized wing and wake for combined panel method/boundary layer calculation. A system of images is used to represent the geometry on the other side of the centerline.

With these assumptions, the discrete integral equation defines a system of linear equations for the unknown values of the perturbation potential on each body panel.

$$\sum_{j=1}^{N_p} D_{ij}\phi_j + \sum_{m=1}^{M} W_{im}\Big(\Delta\Phi\Big)_m = \sum_{j=1}^{N_p} B_{ij}\Big(\frac{\partial\phi}{\partial n}\Big)_j \text{; for i = 1, } N_p, \tag{2.13}$$

where M is the number of spanwise panels and N_p is the total number of panels on the body. Since the strength of the m^{th} streamwise dipole strip, $(\Delta\Phi)_m$, can be related to the potential values on the body, (2.13) is sufficient to determine the unknown potential values.

The influence coefficients are defined as

$$D_{ij} = \frac{1}{4\pi}\left(\iint_{S_j} \mathbf{n}_\xi \cdot \nabla G(\mathbf{x};\xi)d\xi - 2\pi\delta_{ij}\right) \tag{2.14}$$

$$B_{ij} = \frac{1}{4\pi}\iint_{S_j} G(\mathbf{x};\xi)d\xi \tag{2.15}$$

$$W_{im} = \frac{1}{4\pi}\iint_{S_m} \mathbf{n}_\xi \cdot \nabla G(\mathbf{x};\xi)d\xi \tag{2.16}$$

where D_{ij} is the induced potential at panel i due to a unit strength, uniform dipole distribution on the j^{th} body panel, B_{ij} is the induced potential at panel i due to a unit strength, uniform source distribution, and W_{im} is the induced potential at panel i due to the m^{th} streamwise dipole strip in the wake. δ_{ij} is equal to 1 for i=j and 0 otherwise. The influence coefficients, which depend only on the geometry of the body and wake panels, are evaluated analytically using RPAN [39].

2.2.3 Numerical Kutta Condition

In the absence of viscosity a Kutta condition fixes the circulation distribution which will keep the velocity finite at the trailing edge. The numerical implementation of three-dimensional Kutta conditions for potential-based panel methods has been considered extensively for steady flow [24, 18, 26, 44]. It is reviewed here because the Kutta condition must be applied to the outer flow in the coupled potential/boundary layer calculation.

An approximate Kutta condition, developed by Morino and Kuo for 2-D potential-based panel methods [37], requires the strength of the wake dipole sheet to be equal to the difference of the dipole panel strengths located on either side of the foil trailing edge. Recalling that the potential induced by a constant strength dipole panel is equivalent to that induced by a vortex loop along the panel boundary of the same

strength [21], the Morino condition implies that the net vortex strength at the trailing edge is zero.

The strength of the trailing edge dipole panel is evaluated at the panel centroid, not at the trailing edge itself. If the trailing edge has finite thickness, the free-stream potential at the control points on opposite sides of the trailing edge may be different. Lee [31] applied a correction to the Morino condition accounting for this possibility; the modified condition, known as the modified Morino condition, is

$$\Delta\Phi = \Phi^u - \Phi^l = \phi^u - \phi^l + \mathbf{U}_\infty \cdot \mathbf{r}_{t.e.} \tag{2.17}$$

where $\mathbf{r}_{t.e.}$ is the radius vector between collocation point of the trailing edge panels of strip m. The radius vector originates at the lower panel.

The strengths of the wake dipole strips are related to the potential values at the trailing edge (TE) by (2.17). The Kutta condition is incorporated into the system of equations by combining the wake and body influence coefficients.

$$A_{ij} = \begin{cases} D_{ij} - W_{im} & \text{if j corresponds to lower TE panel in strip m} \\ D_{ij} + W_{im} & \text{if j corresponds to upper TE panel in strip m} \\ D_{ij} & \text{otherwise} \end{cases} \tag{2.18}$$

The remaining term, $W_{im}(\mathbf{U}_\infty \cdot \mathbf{r}_{t.e.})_m$, is included as a correction on the right hand side of the system of equations.

In a steady two-dimensional flow, the modified Morino condition is sufficient to ensure pressure equality at the trailing edge. However, its use may lead to pressure mismatches at the trailing edge in three-dimensional flow, especially near the tip. This is generally attributed to the spanwise component of flow along the trailing edge.

Kerwin et al [24] developed an iterative pressure Kutta (IPK) condition which explicitly set the pressure jump across the trailing edge panels to zero. The method solves (2.13) with the wake strength initially set using the modified Morino condition. The wake dipole strength is then adjusted iteratively until the pressure jump across the trailing edge panels is zero. This is equivalent to changing the spanwise circulation distribution.

Use of the IPK condition can result in large changes in the spanwise circulation distribution, or possibly cause the solution to diverge, near the tips of some geometries

[24]. Hsin et al [18] and Kinnas et al [26] have examined the effect of alternate gridding arrangements on the tip solution. The flow adapted grid, introduced by Kinnas et al [26], improved the convergence of the IPK condition and the behavior of the solution near the tip [45]. Pyo [44] latter included wake sheet roll-up with the flow adapted grid and found that the circulation distributions obtained with the modified Morino and iterative pressure Kutta conditions were very similar. His results suggest that proper grid alignment may eliminate the need for the iterative pressure condition altogether.

Only the modified Morino Kutta condition (2.17) is implemented in the present method for the following reasons. First, the IPK condition affects the base inviscid solution by modifying the spanwise circulation distribution. The dipole influence coefficient matrix A, which enforces the Kutta condition, is unchanged. Therefore, the IPK will not affect the viscous correction to the outer flow. Second, velocities are calculated at the trailing edge nodes in the present method, but the IPK ensures pressure equality at the trailing edge panel centroids. It is likely that a solution obtained with the IPK condition would exhibit a pressure mismatch at the trailing edge itself.

2.3 Calculation of Surface Velocities

The potential is defined pointwise at the centroid of each panel by the solution of (2.13). If the potential is assumed continuous, with continuous first order partial derivatives, it may be differentiated to obtain the perturbation velocities tangent to the surface. The algorithm outlined next makes use of the B-spline expansion to compute the surface velocities at the panel nodes.

2.3.1 Formulation

Numerical differentiation of the potential is carried out in the B-spline parametric space. The gradient of ϕ in the s direction is given by the divergence theorem

$$\oint_C \phi dt = -\iint_S \frac{\partial \phi}{\partial s} dS, \tag{2.19}$$

where C is a closed curve joining the centroids of the four panels, traversed in the counter clockwise direction as shown in Figure 2-5. S is the area contained within

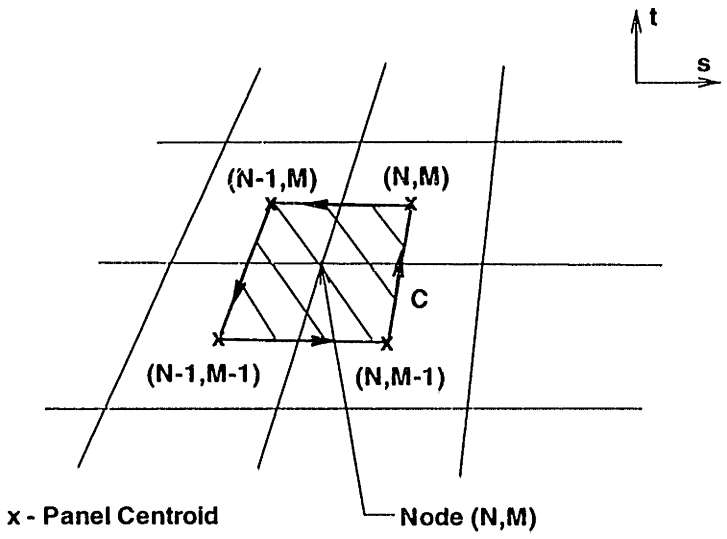

Figure 2-5: Definition of the contour in the B-spline parametric domain for surface derivative calculations. Double indices are used to specify the panels and nodes.

C. Rearranging (2.19), with the assumption that the derivative is constant inside the contour,

$$\frac{\partial \phi}{\partial s} = -\frac{1}{S} \oint_c \phi dt \tag{2.20}$$

The discrete form of (2.20) is equivalent to a central difference first derivative on a uniform grid (in the parametric space) provided that the average values of the potential $\frac{\phi_{N-1,M-1}+\phi_{N-1,M}}{2}$ and $\frac{\phi_{N,M-1}+\phi_{N,M}}{2}$ are used. An equivalent expression for $\frac{\partial \phi}{\partial t}$ is

$$\frac{\partial \phi}{\partial t} = \frac{1}{S} \oint_c \phi ds \tag{2.21}$$

The derivatives $\frac{\partial \phi}{\partial s}$ and $\frac{\partial \phi}{\partial t}$ do not represent the surface velocities directly because the B-spline transformation includes a scaling factor that varies with position. The scaling factor is properly accounted for if the derivatives are transformed back into global coordinates. The perturbation velocity in body-fixed coordinates is:

$$\mathbf{u} = \frac{\partial \phi}{\partial \mathbf{X}} \tag{2.22}$$

which may be expanded in terms of $\frac{\partial \phi}{\partial s}$ and $\frac{\partial \phi}{\partial t}$ by the chain rule,

$$\frac{\partial \phi}{\partial \mathbf{X}} = \frac{\partial \phi}{\partial s}\frac{\partial s}{\partial \mathbf{X}} + \frac{\partial \phi}{\partial t}\frac{\partial t}{\partial \mathbf{X}} \tag{2.23}$$

where $\frac{\partial s}{\partial \mathbf{X}}$ and $\frac{\partial t}{\partial \mathbf{X}}$ are the first two columns of the transformation matrix derived in Appendix A. Finally, the perturbation velocities in surface coordinates are found by

projecting $\mathbf{u}$ into the directions defined by the two unit tangent vectors, $e_{\hat{x}}$ and $e_{\hat{z}}$.

$$u_e = \mathbf{u} \cdot e_{\hat{x}} \tag{2.24}$$

$$w_e = \mathbf{u} \cdot e_{\hat{z}}$$

The total velocity is found by combining the perturbation velocities with the inflow velocity after it has been projected into surface coordinates.

The pressure is calculated from the total velocity using Bernoulli's equation and expressed as a non-dimensional pressure coefficient

$$C_p = \frac{p - p_\infty}{\frac{\varrho}{2} U_\infty^2} \tag{2.25}$$

2.3.2 Treatment of Boundary Nodes

Ghost field points are introduced outside the edges of the grid, except at the wing and wake tip boundaries, to close the contour around boundary nodes. Figure 2-6 presents a computational grid for a wing, with the positions of the ghost field points marked.

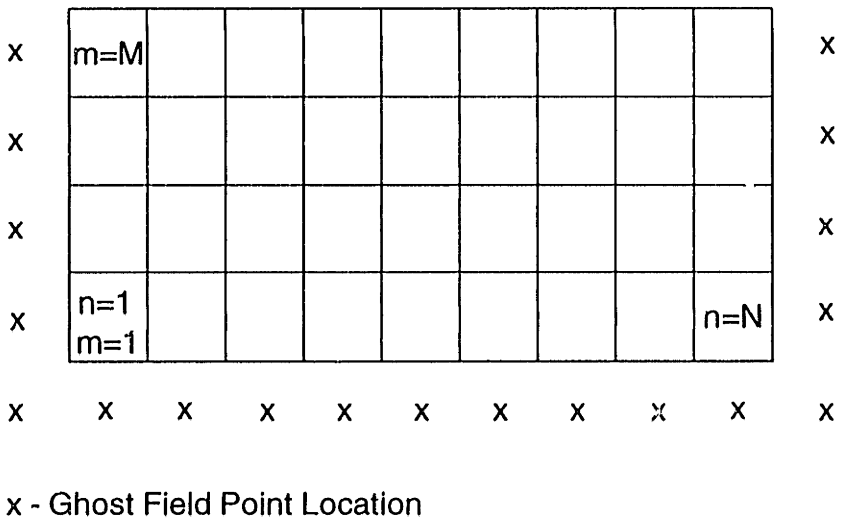

Figure 2-6: Computational grid showing ghost field point locations for a wing. n is the chordwise panel index and m is the spanwise panel index.

The boundaries along n=1 and n=N represent the trailing edge on the lower and upper surfaces of the wing respectively. Ghost field points are placed at the centroids of the first streamwise wake panels along these edges. The potential assigned to each

field point is given by (2.4) with T = 1 and also includes the potential jump due to the wake dipole sheet. Half of the potential jump $(\Delta\Phi)_m$ is subtracted from the mean potential at ghost points along n=1 and added at ghost points along n=N. The potential is continuous across the trailing edge (along a streamline) because the Kutta condition removes the singularity. Therefore, it can be differentiated numerically to calculate the perturbation velocities at trailing edge nodes.

The boundary along m=1 lies on an image plane for the cases in this thesis. The potential assigned to ghost points along this boundary satisfy a Neumann condition to ensure the flow is parallel to the boundary.

$$\frac{\partial \phi}{\partial Y} = 0 \tag{2.26}$$

The reasons for introducing additional field points instead of using a one-sided difference formula are discussed in §4.3.

2.4 Numerical Validation of the Panel Method

Computational results obtained for an annular wing are presented here to demonstrate that our panel method and the algorithm used to compute surface velocities are implemented correctly. Our calculations are compared with results presented by Kerwin et al [24] who used a similar low order potential-based panel method developed by Lee [31]. The results which follow show that predictions made with the two codes agree well.

The test geometry is a long duct, formed by revolving a NACA 0010 section set at zero angle of attack at a mean radius of 0.1 chords. Predicting the pressure distribution for this geometry is a demanding test of the panel code because the mass flow through the duct, which is set by the Kutta condition, is extremely high.

A paneled representation of the duct is shown in Figure 2-7. The grid is cosine-spaced in the chordwise direction, with clustering at the nose and tail, and equally-spaced around the circumference of the duct. Calculations were made for discretizations with 36 panels around the airfoil section and 9, 18, 36, and 60 panels around the circumference. The entire duct was paneled instead of exploiting symmetry in the circumferential direction. All calculations were made for a unit inflow aligned with the duct centerline.

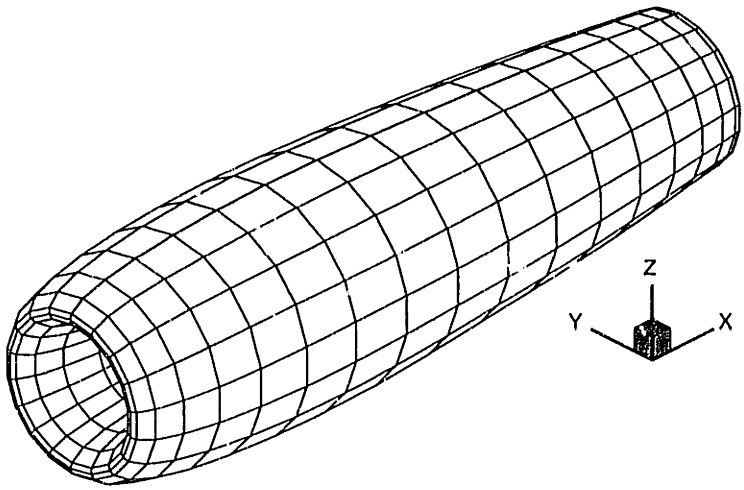

Figure 2-7: Panel arrangement for an annular wing formed from a NACA 0010 section with a chord/mean radius ratio of ten. The discretization shown has 36 panels around the airfoil section and 18 panels around the circumference

Pressure distributions computed with the current method are shown in Figure 2-8 and results from Kerwin et al [24] are shown in Figure 2-9. The pressure distributions computed with the current method are in good agreement with the published results for each discretization. The minimum pressure coefficient of -11.3, computed for the 36x60 grid, is identical to the value published by Kerwin, but higher than the converged numerical solution of -13.8 which was computed with a high order axisymmetric panel method [24]. Note that the finest discretization shown in Figure 2-9 was not analyzed with the current method.

Valentine [51] used the VSAERO/E0 panel code to analyze this duct and reported a minimum pressure coefficient of -15.2. This is about 10% lower than the converged value.

The panel distribution obtained by cosine-spacing panels around the airfoil section has large gradients near the leading and trailing edges. Uniform grids are more suitable for boundary layer calculations [11]. Three additional calculations were made with a panel distribution more typical of one used for a coupled potential flow/boundary layer calculation. Each grid contained 91 panels around the airfoil section, spaced using a linear blending algorithm [25]. The number of circumferential panels was varied from 9 to 36.

Pressure distributions are shown in Figure 2-10 for these computations. The distributions are similar to those obtained for the cosine-spaced grid. The minimum pressure coefficient is closer to the converged value since the grid has been refined in the chordwise direction, but none have converged to the proper value.

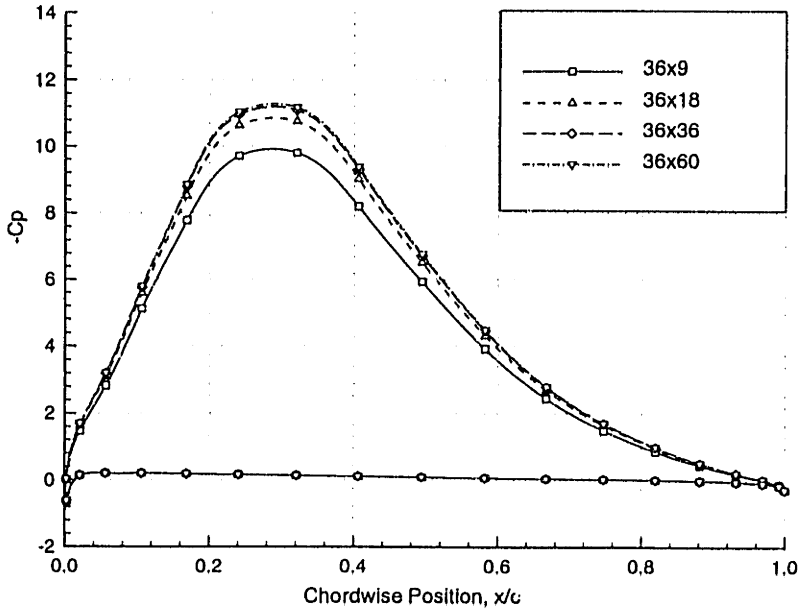

Figure 2-8: Computed pressure distributions for the nacelle obtained with the current panel method for various paneling arrangements

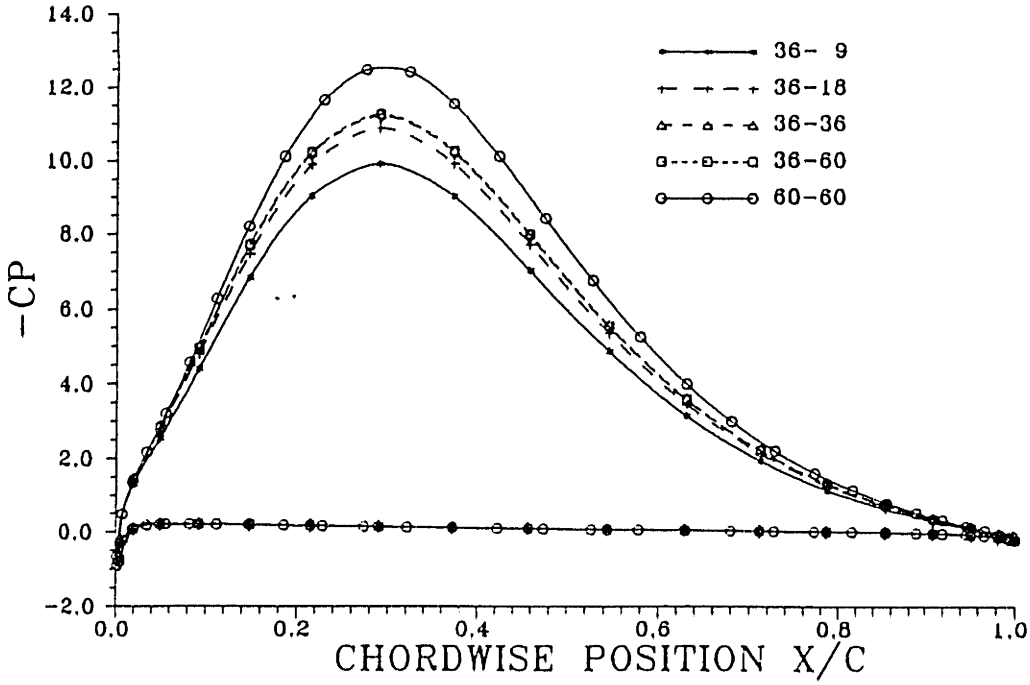

Figure 2-9: Pressure distributions for the nacelle published by Kerwin et al [24]

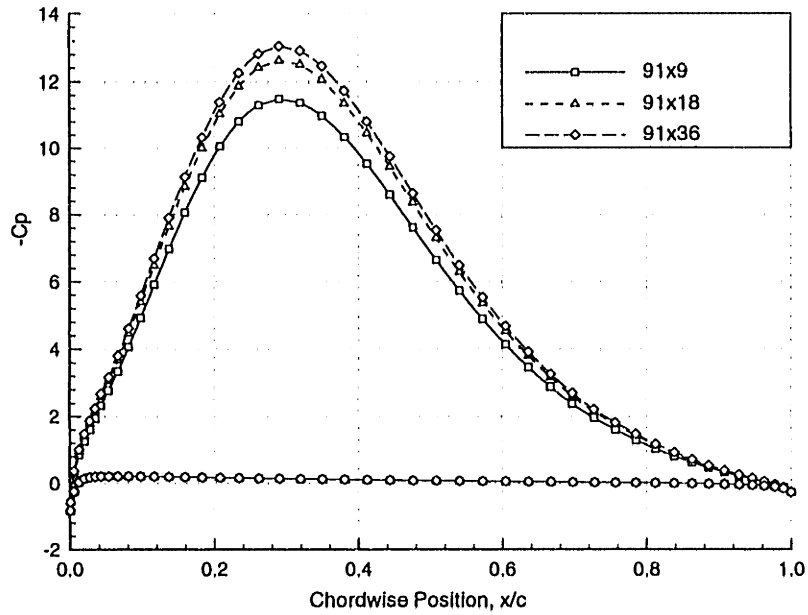

Figure 2-10: Computed pressure distributions for the nacelle with panels distributed around the airfoil section using a linear blending algorithm

Chapter 3

Three-Dimensional Integral Boundary-Layer Equations

3.1 Overview

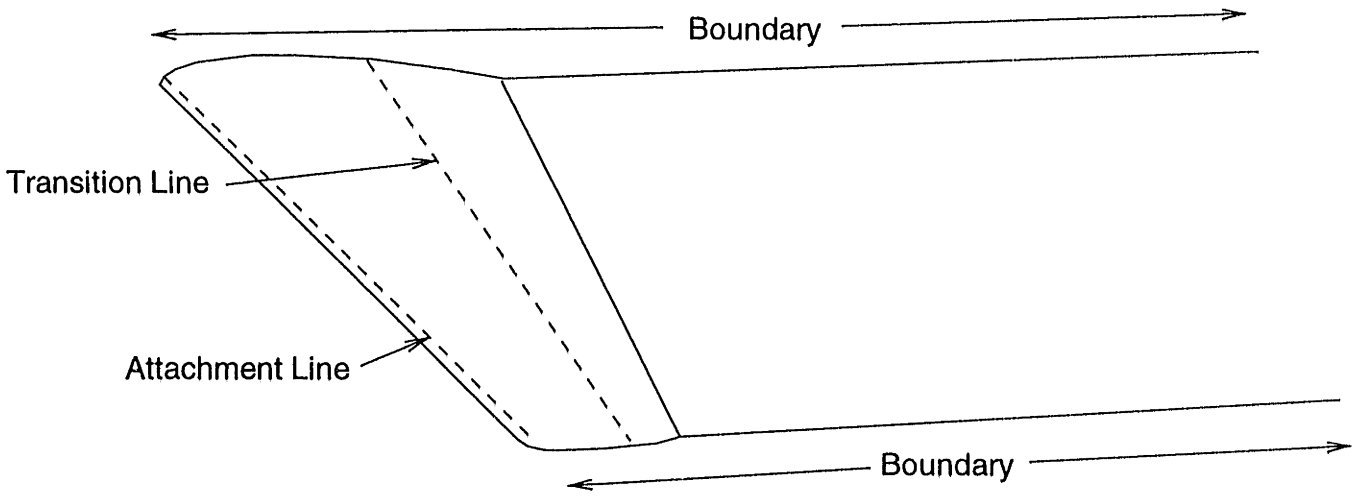

Figure 3-1: Boundary Layer Domain

The viscous flow in the boundary layer and wake is modeled using the three-dimensional integral boundary-layer equations. The purpose of this chapter is to present the mathematical and numerical formulations used in the current work. The following presentation is based on Nishida's formulation [41] with the essential difference being in the treatment of the velocities at the outer edge of the boundary layer.

Figure 3-1 shows a typical boundary-layer domain. The integral boundary layer equations are applied on the upper and lower surfaces of wing and along the wake.

The hyperbolic nature of the boundary-layer equations imposes requirements on the numerical method used to solve the equations, on the boundary conditions that are applied along the edges of the domain, and on the initial conditions that are specified along the attachment and transition lines.

3.2 Mathematical Formulation

The boundary layers that form around lifting surfaces at high Reynolds numbers are generally thin compared to the chord length, even when a modest amount of flow separation is present. To leading order, the pressure is constant through the boundary layer, and shear stresses normal to the wall and the effects of velocities normal to the wall on the shear stresses are inconsequential. With these assumptions, the Navier-Stokes equations simplify to the thin shear layer equations [55].

The three-dimensional integral boundary layer equations are derived by integrating linear combinations of the continuity and thin shear layer equations across the boundary layer in the direction normal to the wall. Details of this derivation are presented in [38] for compressible flow. For incompressible flow these equations, in terms of Cartesian coordinates, are:

x Momentum equation

$$\frac{\partial}{\partial x}(\rho q_e^2 \theta_{xx}) + \frac{\partial}{\partial z}(\rho q_e^2 \theta_{xz}) + \rho q_e \delta_x^* \frac{\partial u_e}{\partial x} + \rho q_e \delta_z^* \frac{\partial u_e}{\partial z} = \tau_{xw} \tag{3.1}$$

z Momentum equation

$$\frac{\partial}{\partial x}(\rho q_e^2 \theta_{zx}) + \frac{\partial}{\partial z}(\rho q_e^2 \theta_{zz}) + \rho q_e \delta_x^* \frac{\partial w_e}{\partial x} + \rho q_e \delta_z^* \frac{\partial w_e}{\partial z} = \tau_{zw} \tag{3.2}$$

Kinetic energy equation

$$\frac{\partial}{\partial x}(\rho q_e^3 \theta_x^*) + \frac{\partial}{\partial z}(\rho q_e^3 \theta_z^*) = 2\mathcal{D} \tag{3.3}$$

Shear stress lag equation

$$\frac{\delta}{C_\tau}\frac{\partial C_\tau}{\partial \xi} = K_c \left({C_\tau^{1/2}}_{eq} - C_\tau^{1/2} \right) \tag{3.4}$$

Equations (3.1) and (3.2) are the extension of the von Kármán momentum equation for a two-dimensional boundary layer [55] to three-dimensions. u_e and w_e are the edge velocities in the x and z directions, q_e is the magnitude of the edge velocity, and τ_{xw} and τ_{zw} are the components of the wall shear stress. Definitions of the momentum

thicknesses, $(\theta_{xx}, \theta_{xz}, \theta_{zx}, \theta_{zz})$, and displacement thicknesses, (δ_x^*, δ_z^*), are presented in Appendix B. The density at the edge of the boundary layer, ρ, is included in the formulation for dimensional consistency. Since the fluid is incompressible and the equations are solved in non-dimensional form, the density can be set to unity and dropped from the formulation. The momentum equations express a balance between momentum flux deficit, pressure forces, and surface shear stresses in the shear layer.

An additional equation is used with the momentum equations to permit calculation of non-equilibrium boundary layers. In a non-equilibrium boundary layer, the shape parameter and the boundary layer shear-stress profile are a function of position due to pressure gradient variations in the external flow. The kinetic energy equation (3.3), which expresses conservation of energy in the boundary layer, is used as the auxiliary equation for the calculations described in this thesis. The definitions of the kinetic energy thicknesses, θ_x^* and θ_z^*, and dissipation integral, $\mathcal{D}$, are given in Appendix B. The entrainment equation is sometimes used as the auxiliary equation [49] [13], but is not considered here.

The transport equation (3.4) for the maximum shear stress coefficient completes the system of equations. This equation accounts for history effects in the outer layer of a non-equilibrium turbulent boundary layer. C_τ is the shear stress coefficient, $C_{\tau eq}$ is the equilibrium shear stress coefficient, and ξ is the lag direction which is taken in the chordwise direction. K_c is an empirical coefficient equal to 5.6 as suggested by Green [12]. The equation is a correction to the boundary-layer formulation which has been found to improve the agreement between prediction and experiment.

3.3 Coordinate Systems

The three-dimensional integral boundary-layer equations are generally solved in a curvilinear surface coordinate system. The formulations presented by Groves [13] and Cousteix [7] use an orthogonal, curvilinear coordinate system based on the local streamline direction. One coordinate is defined by the projection of the outer streamline onto the surface; the second is taken orthogonal to it and tangent to the surface. This coordinate system is introduced because the empirical correlations that are required in a three-dimensional integral boundary-layer formulation are defined in this system. The coordinate system is called the streamwise-crossflow, or *1-2*, coordinate

system here.

Equations (3.1)-(3.4) are written for a Cartesian coordinate system. Metric terms that account for the curvature of the grid are required if the equations are formulated in curvilinear coordinates. For a general surface, the metrics must be evaluated numerically, imposing the condition that the surface is discretized using smooth grid lines. The metrics must also be recomputed if the direction of the outer streamline is permitted to change.

The boundary-layer formulation presented here uses the approach developed by Mughal [38] to account for the curvature of the grid lines. A local Cartesian coordinate system is introduced at each panel. After the boundary-layer variables are evaluated in streamwise-crossflow coordinates at the four corner nodes, they are rotated into the common local Cartesian coordinates before the equations are assembled. The rotation terms introduced in going from the *1-2* to the x-z systems in effect replace the coordinate metric terms which appear in the *1-2* equations. Working with the x-z coordinates has the great advantage that the surface grid is fixed and arbitrary.

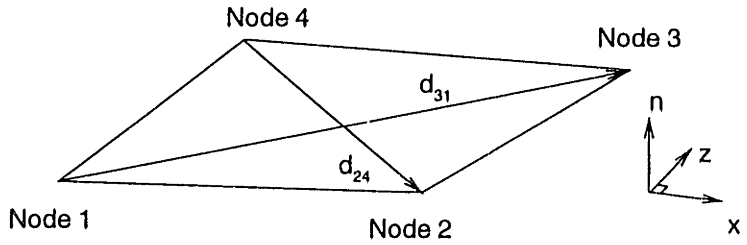

Figure 3-2: Local panel x-z coordinates.

The local panel coordinate system is shown in Figure 3-2. x is parallel to the chordwise edge of the panel, n is normal to the surface pointing into the flowfield, and z lies in the surface, orthogonal to the other two directions. The panel coordinate system is constructed by projecting the 3-D surface onto the plane defined by the unit vectors $\hat{\mathbf{e}}_x$ and $\hat{\mathbf{e}}_z$ which are the direction cosines between the local 2-D and the global body-fixed coordinate systems. $\hat{\mathbf{e}}_x$ is directed along the chordwise panel edge and $\hat{\mathbf{e}}_z$ is orthogonal to $\hat{\mathbf{e}}_x$ and the panel unit normal, $\hat{\mathbf{e}}_n$.

$$\hat{\mathbf{e}}_z = \hat{\mathbf{e}}_n \times \hat{\mathbf{e}}_x \tag{3.5}$$

The normal vector is calculated by the cross product of the diagonals connecting

opposite corners of the panel. The nodes are numbered so the normal always points out into the flow.

$$\hat{\mathbf{e}}_n = \frac{\mathbf{d}_{24} \times \mathbf{d}_{31}}{|\mathbf{d}_{24} \times \mathbf{d}_{31}|} \tag{3.6}$$

Choosing x to be parallel to one edge of the panel is done for convenience. The boundary-layer equations are rotationally invariant, and any other orientation of the x-z axes would be adequate.

3.4 Primary Variables

The boundary-layer variables expressed in local panel coordinates are not suitable for use as primary variables because each panel surrounding a node may have a different coordinate system. Primary variables are selected from variables defined in the streamline coordinate system since they are uniquely defined at each node. In addition, secondary variables which are derived from primary variables are always defined in the streamwise coordinates.

Four independent primary variables must be selected because there are four boundary-layer equations. In the current formulation the primary boundary-layer variables are chosen as $C_\tau^{1/2}, \theta_{11}, m_1, m_2$. $C_\tau^{1/2}$ is the square root of the shear stress coefficient, θ_{11} is the streamwise component of the momentum thickness, and m_1 and m_2 are the streamwise and crossflow components of the mass defect respectively. The mass defects are defined as:

$$m_1 \equiv \rho q_e \delta_1^* \qquad\qquad m_2 \equiv \rho q_e \delta_2^*, \tag{3.7}$$

where q_e is the magnitude of the edge velocity, δ_1^* is the streamwise component of displacement thickness, and δ_2^* is the crossflow component of displacement thickness. The two components of mass defect are selected as primary variables to reduce the number of unknowns at each node.

δ_1^*, δ_2^*, u_e, and w_e are not primary variables in the present formulation and must be related to the mass defect. Expressions for the displacement thicknesses follow directly from (3.7). Equations for the edge velocities are derived in Chapter 4.

The remaining variables in the boundary-layer equations are expressed in terms of $C_\tau^{1/2}, \theta_{11}, \delta_1^*$, and δ_2^* by the closure relations listed in Appendix B. The streamwise closure relations are developed from assumed forms of two-dimensional velocity profiles and empirical skin-friction and dissipation relations. Crossflow thicknesses are

related to the streamwise thicknesses using the outer part of the Johnston triangular crossflow velocity profile [38].

Boundary layer quantities are rotated from streamline coordinates into the panel coordinate system using a 2-D rotation about the panel normal. The transformations from *1-2* coordinates to local Cartesian coordinates are listed in Appendix B.

3.5 Numerical Implementation

A system of discrete equations is derived by applying a Petrov-Galerkin Finite Element Method (FEM) to (3.1)-(3.4), following standard procedures that are found in references on the FEM [15] [19]. The Petrov-Galerkin formulation, which selects different weighting and shape, or basis, functions, is used to introduce upwinding into the numerical formulation. This section briefly describes the shape functions and presents a derivation of discrete equations using the method of weighted residuals.

3.5.1 Element Description

In a finite element calculation the continuous surface is replaced by a collection of discrete elements. For the calculations described here, the elements are the quadrilateral panels used in the panel method calculation described in §2.2.2. A computational coordinate system is introduced on each panel to facilitate calculations at the elemental level. Figure 3-3 shows a quadrilateral element in the local panel and natural coordinate systems. The element maps to a square in natural coordinates with corners at $\xi = \pm 1$, $\eta = \pm 1$ although it may be distorted in physical coordinates,

The mapping function for an isoparametric element is the shape function. A point (ξ, η) is mapped to physical coordinates by:

$$\mathbf{x}(\xi, \eta) = \sum_{j=1}^{4} N_j^e(\xi, \eta)\mathbf{x}_j \tag{3.8}$$

where the $\mathbf{x}_j$ are the local 2-D Cartesian coordinates and N_j^e is the shape function associated with the j^{th} vertex of the element. Bilinear shape functions are used in the current boundary-layer FEM formulation.

$$N_j^e(\xi, \eta) = \frac{1}{4}(1 + \xi\xi_j)(1 + \eta\eta_j) \tag{3.9}$$

ξ_j and η_j are the natural coordinates of the j^{th} vertex of the element.

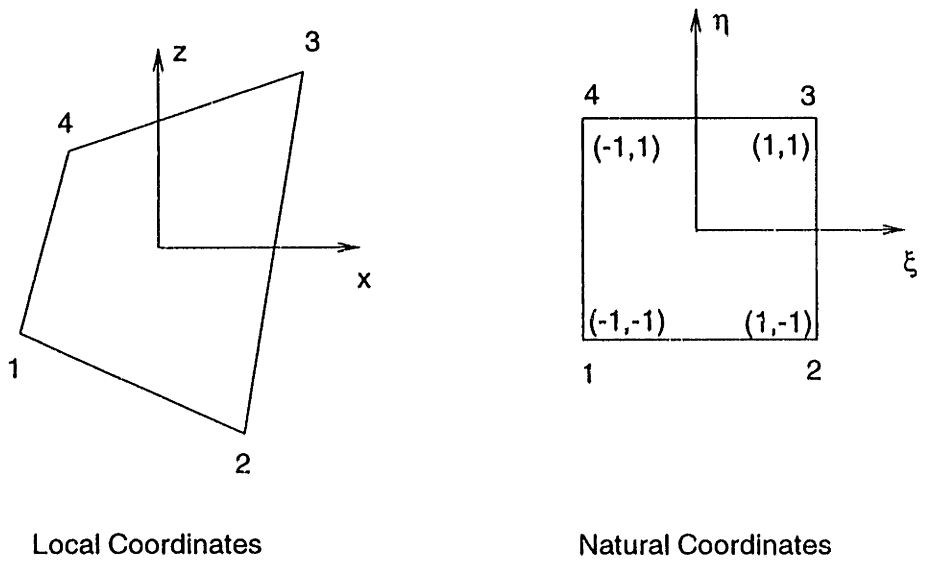

Figure 3-3: Quadrilateral isoparametric element in local and natural coordinate systems.

Nodal values of the boundary-layer variables vary linearly over an element. At the point (ξ, η) on the element, the variable is approximated as

$$\tilde{\varphi}(\xi,\eta) = \sum_{j=1}^{4} N_j^e(\xi,\eta)\varphi_j \tag{3.10}$$

where φ is one of the terms in (3.1)-(3.4), e.g. $(\rho q_e \delta_x^* \frac{\partial u_e}{\partial x})$.

The boundary-layer equations include terms which require the evaluation of the gradient in the local Cartesian coordinate system. Since the boundary layer variables are linear functions within an element, their derivatives can be calculated. For example, the x derivative of φ is determined from the nodal values of φ and the derivatives of the element shape functions.

$$\frac{\partial \tilde{\varphi}}{\partial x}(\xi,\eta) = \sum_{j=1}^{4} \frac{\partial N_j^e}{\partial x}(\xi,\eta)\varphi_j \tag{3.11}$$

The gradient of a shape function in physical coordinates is calculated by expanding derivatives of the shape function in natural coordinates by the chain rule and solving the following system of equations for $\frac{\partial N}{\partial x}$ and $\frac{\partial N}{\partial z}$.

$$\begin{bmatrix} \frac{\partial x}{\partial \xi} & \frac{\partial z}{\partial \xi} \\ \frac{\partial x}{\partial \eta} & \frac{\partial z}{\partial \eta} \end{bmatrix} \begin{Bmatrix} \frac{\partial N}{\partial x} \\ \frac{\partial N}{\partial z} \end{Bmatrix} = \begin{Bmatrix} \frac{\partial N}{\partial \xi} \\ \frac{\partial N}{\partial \eta} \end{Bmatrix} \tag{3.12}$$

The elements of the Jacobian matrix are calculated by differentiating (3.8) with re-

spect to ξ and η.

$$\frac{\partial x}{\partial \xi} = \sum_{j=1}^{4} \frac{\partial N_j^e}{\partial \xi} x_j \qquad \frac{\partial x}{\partial \eta} = \sum_{j=1}^{4} \frac{\partial N_j^e}{\partial \eta} x_j \tag{3.13}$$
$$\frac{\partial z}{\partial \xi} = \sum_{j=1}^{4} \frac{\partial N_j^e}{\partial \xi} z_j \qquad \frac{\partial z}{\partial \eta} = \sum_{j=1}^{4} \frac{\partial N_j^e}{\partial \eta} z_j$$

with

$$\frac{\partial N_j^e}{\partial \xi} = \frac{1}{4}(1+\xi_j)(1+\eta\eta_j) \tag{3.14}$$
$$\frac{\partial N_j^e}{\partial \eta} = \frac{1}{4}(1+\xi\xi_j)(1+\eta_j)$$

3.5.2 Weighting Function

The current method uses the weighting scheme proposed by Nishida [41] to provide an upwind discretization of the equations.

$$W_1^e = 0, \qquad W_2^e = \frac{1}{2}(1-\eta), \qquad W_3^e = \frac{1}{2}(1+\eta), \qquad W_4^e = 0 \tag{3.15}$$

This choice of weighting function provides upwinding in the ξ direction and central differencing in the spanwise direction. Upwinding is required to prevent the oscillations which arise in the solution of hyperbolic equations when central difference discretizations are used [16]. Neither Mughal [38] or Nishida required crosswind dissipation with this weighting function.

3.5.3 Discrete Equations

Discrete equations are derived at each node using the method of weighted residuals. The procedure consists of the following steps.

1. Approximate the continuous distribution of boundary-layer variables in (3.1)-(3.4) using the nodal values and the shape functions described in the §3.5.1. Nodal values of the variables in the panel x-z coordinate system are calculated from the streamline-crossflow variables using the identities listed in §B.2.

2. Substitute the approximations into the continuous equations. Since the approximations will generally not satisfy the continuous equations, a residual is formed by taking the difference between the two sides of the equation.

3. Integrate the residual equations over the body and wake surfaces after multiplying by the weighting function described in §3.5.2.

4. A solution to the boundary layer equations is found by driving the weighted residuals to zero using Newton's method as will be described in Chapter 5.

The elemental weighted residual equations are:

Shear Stress Lag Equation

$$\iint_{\partial\Omega} W\Big\{2\sum_i N_i^e(\delta)_i \sum_j \frac{\partial N_j^e}{\partial \xi}\Big(\log C_\tau^{1/2}\Big)_j - K_c \sum_j N_j^e\Big((C_\tau^{1/2}{}_{eq})_j - (C_\tau^{1/2})_j\Big)\Big\} dS = R_{C_\tau^{1/2}} \tag{3.16}$$

Kinetic Energy Equation

$$\iint_{\partial\Omega} W\Big\{\sum_i \frac{\partial N_i^e}{\partial x}(\rho q_e^3 \theta_x^*)_i + \sum_i \frac{\partial N_i^e}{\partial z}(\rho q_e^3 \theta_z^*)_i - 2\sum_i N_i^e(\mathcal{D})_i\Big\} dS = R_{k.e.} \tag{3.17}$$

x Momentum Equation

$$\begin{aligned}\iint_{\partial\Omega} W\Big\{&\sum_i \frac{\partial N_i^e}{\partial x}(\rho q_e^2 \theta_{xx})_i + \sum_i \frac{\partial N_i^e}{\partial z}(\rho q_e^2 \theta_{xz})_i \\ &+ \textstyle\sum_i N_i^e(\rho q_e \delta_x^*)_i \sum_j \frac{\partial N_j^e}{\partial x}(u_e)_j \\ &+ \textstyle\sum_i N_i^e(\rho q_e \delta_z^*)_i \sum_j \frac{\partial N_j^e}{\partial z}(u_e)_j - \sum_i N_i^e(\tau_{x_w})_i\Big\} dS = R_{x.m.}\end{aligned} \tag{3.18}$$

z Momentum Equation

$$\begin{aligned}\iint_{\partial\Omega} W\Big\{&\sum_i \frac{\partial N_i^e}{\partial x}(\rho q_e^2 \theta_{zx})_i + \sum_i \frac{\partial N_i^e}{\partial z}(\rho q_e^2 \theta_{zz})_i \\ &+ \textstyle\sum_i N_i^e(\rho q_e \delta_x^*)_i \sum_j \frac{\partial N_j^e}{\partial x}(w_e)_j \\ &+ \textstyle\sum_i N_i^e(\rho q_e \delta_z^*)_i \sum_j \frac{\partial N_j^e}{\partial z}(w_e)_j - \sum_i N_i^e(\tau_{z_w})_i\Big\} dS = R_{z.m.}\end{aligned} \tag{3.19}$$

The integral over each element is calculated numerically using 2x2 Gauss quadrature. In (3.16), C_τ is replaced with $C_\tau^{1/2}$ using the relation:

$$\frac{1}{C_\tau}\frac{\partial C_\tau}{\partial \xi} = \frac{\partial}{\partial \xi}(\log C_\tau) = 2\frac{\partial}{\partial \xi}\left(\frac{1}{2}\log C_\tau\right) = 2\frac{\partial}{\partial \xi}\left(\log C_\tau^{1/2}\right) \tag{3.20}$$

and the gradient of the shape function in the ξ direction is calculated as:

$$\frac{\partial N_i}{\partial \xi} = \frac{\partial N_i}{\partial x}(\hat{\mathbf{e}}_x \cdot \hat{\mathbf{e}}_\xi) + \frac{\partial N_i}{\partial z}(\hat{\mathbf{e}}_z \cdot \hat{\mathbf{e}}_\xi) \tag{3.21}$$

The ξ direction is approximated as the chordwise direction.

3.6 Boundary Conditions

The three-dimensional integral boundary-layer equations (3.1)-(3.3) are a set of coupled first order hyperbolic partial differential equations, and therefore, admit solutions that are wave-like. The direction of propagation of the solution is determined by the characteristic roots of the equations. There are three characteristic directions associated with the integral boundary layer equations: one is in the direction of the limiting wall streamline, one is approximately in the direction of the outer streamline, and the third lies in between the two [7]. Conditions must be specified at locations where the characteristics enter the boundary-layer computational domain. This includes the attachment line, where the outer flow dividing streamline is assumed to attach the airfoil section, and the wing tip. A Neumann boundary condition is also required at image planes to enforce the symmetry condition.

3.6.1 Attachment Line

For the examples considered in this thesis, the flow at the attachment line is approximated as the flow along the attachment line of an infinite swept wing. If η is the coordinate parallel to the leading edge and ξ the coordinate normal to it, the edge velocities at the leading edge of an infinite swept wing are [7]:

$$u_e = k\xi \qquad\qquad w_e = w_\infty = \text{const} \tag{3.22}$$

In this coordinate system the continuity and ξ momentum equations decouple from the η momentum equation [55]. The problem can be solved by treating the flow in the ξ direction as an equivalent 2-D flow, which for an infinite swept wing, is simply the solution for a 2-D stagnation flow.

Values of the streamwise displacement and momentum thicknesses are set at nodes on either side of the attachment line using the 2-D Falkner-Skan similarity solution.

$$\theta_{11} = C_\theta \sqrt{\frac{\xi}{Re_\infty u_\xi}} \qquad\qquad \delta_1^* = C_{\delta^*} \sqrt{\frac{\xi}{Re_\infty u_\xi}} \tag{3.23}$$

ξ is the distance from the attachment line to the node, in the direction normal to the leading edge, u_ξ is the component of the edge velocity in this direction, and Re_∞ is the Reynolds number based on the freestream velocity. The crossflow mass defect, hence the crossflow displacement thickness, is assumed to be zero, approximating two-dimensional flow. $C_\tau^{1/2}$ is set to zero because the flow is laminar.

The coefficients in (3.23) depend on the local pressure gradient in the ξ direction and in theory can be determined as part of the solution. In the present implementation, the coefficients C_θ and C_{δ^*} are assigned values of 0.38574 and 0.90649 respectively, which corresponds to a flow with a shape factor, H, of 2.35. Stagnation flow conditions (H=2.21,C_θ=0.29234, C_{δ^*}=0.64791) were used originally, but sometimes prevented the boundary-layer equations from converging at nodes immediately downstream of the similarity region, especially if this short region was not resolved adequately. The pressure gradient implied by the similarity solution was incompatible with the one obtained from the approximate solution of the integral boundary-layer equations on the coarse grid. When the coefficients were increased, the convergence problems were alleviated. The boundary-layer solution for most of the wing is insensitive to the initial conditions in any event.

The surface coordinate system defined in Figure 2-3 wraps around the airfoil section. When the chordwise chordwise edge velocity is transformed to this coordinate system, it is negative on the pressure side of the attachment line and positive on the suction side of the attachment line. The attachment point for each spanwise section is found from the zero crossing of the edge velocity in this coordinate system.

3.6.2 Transition Line

A starting solution for $C_\tau^{1/2}$ is required at the transition line and is set using the two-dimensional empirical relation derived by Drela [41].

$$C_\tau^{1/2} = 1.8 \exp\left(\frac{-3.3}{H-1}\right) C_\tau^{1/2}{}_{eq} \tag{3.24}$$

The location of the transition line is specified for all calculations presented in this thesis. Transition is assumed to take place at the first node downstream of the specified location.

3.6.3 Image Plane Boundary Conditions

The flow along an image plane must be parallel to the plane, leading to a symmetry condition, $\frac{\partial}{\partial \eta} = 0$, where η is the direction normal to the plane. This condition is a natural boundary condition in the FEM discretization and is implemented by multiplying the residual equations by two for nodes located on a symmetry boundary.

3.6.4 Tip Boundary Conditions

One way to set boundary conditions for hyperbolic equations is to write the equations in characteristic form and solve for the characteristic roots. One boundary condition must be specified for each characteristic entering the domain. However, determining the characteristic roots of the system of 3-D integral boundary-layer equations is complicated by the empirical closure relations. A more practical approach is generally taken, setting the boundary conditions based on the results of numerical experiments.

Mughal [38] investigated wing tip boundary conditions by calculating a direct mode marching solution to the 3-D integral boundary-layer equations over the surface of a finite wing. The solution at boundary nodes was set, or extrapolated from the interior part of the grid using a zero-gradient or zero-curvature condition. Mughal found that Dirichlet and zero-gradient conditions excited spanwise sawtooth mode, but reasonable results were obtained using the zero-curvature extrapolation scheme.

Nishida [41] examined the problem of boundary conditions using a direct marching, wake calculation. The external flow over the trailing wake of a wing was approximated as the irrotational flow near a stagnation point. Dirichlet, zero-gradient, and an approximate form of characteristic boundary conditions were applied along the side boundaries for the calculations. The last condition assumed that one characteristic pointed out of the domain; δ_2^* was permitted to float while the other boundary-layer variables $(\delta_1^*, \theta_{11})$ were specified. Since the results obtained using this boundary condition were smoother than results obtained with the other conditions, Nishida concluded that this type of boundary condition should be applied at boundary along the suction side of the wing and wake tips.

A condition similar to the one proposed by Nishida was applied in the initial calculations made with the current method. The crossflow component of mass defect, m_2, was allowed to float while the remaining variables were specified. The streamwise components of mass defect and momentum thickness were estimated with a two dimensional boundary-layer solver, using the 3-D inviscid chordwise velocity distribution at the tip as the outer flow. Because solutions obtained with this boundary condition tended to converge slowly and exhibited a non-physical behavior at the tip, the boundary condition was subsequently replaced with a condition that let all of the wing tip variables float. When this boundary condition was used in com-

bination with spanwise numerical smoothing (§5.5), the solution near the tip was found to be reasonable. By allowing the solution to float, the variables associated with outwardly-directed characteristics are not constrained while smoothing prevents variables associated with characteristics entering the domain from growing without bound.

An accurate treatment of the boundary conditions is not essential for the geometries that are analyzed in this thesis because the region of error is limited to the immediate tip area. The region of error is defined by the domain of influence of the nodes along the tip on the suction side. The issue of boundary conditions is more important at the junction of a hull and aft swept keel. If the flow contains a large spanwise component outward from the hull, the boundary condition can affect the entire solution. Computing this would require knowledge of the viscous flow on the hull, and how this viscous flow would influence the corner flow at the keel root. This is beyond the scope of this thesis.

Chapter 4

Edge Velocity Equations

The leading order effect of the boundary layer is to displace the potential flow away from the body by an amount equal to the displacement thickness. In addition to inducing an outward velocity, the boundary layer introduces perturbations in the velocity components parallel to the wall. Early two-dimensional viscous/inviscid interaction (VII) methods approximated the tangential velocity perturbation using an simplified interaction law based on thin airfoil theory [52]. Cebeci et al [4] incorporated an interaction law of this type in their quasi-three-dimensional boundary layer calculations for swept wings.

While the aforementioned interaction law models the local interaction between the boundary layer and potential flows adequately, it does not satisfy the Kutta condition or capture global elliptic interaction. A more accurate representation of the outer flow, one that takes into account the global influence of the inviscid solution and the boundary layer, is obtained by adding blowing sources to an exact model of the inviscid flow. Starting with a two-dimensional linear-vorticity streamfunction panel method, Drela [10] derived an expression for the tangential velocity at the edge of the boundary layer in terms of the known inviscid component and a correction that depends only on the mass defect. Since the potential and boundary layer equations are coupled through the edge velocity, this equation provides the outer boundary condition in the coupled potential flow/boundary-layer calculation. Hufford [20] derived an equivalent expression from the two-dimensional Green's Theorem integral equation for the perturbation potential.

This thesis extends the approach developed by Hufford to three dimensions. Expressions for the edge velocities, u_e and w_e, are derived in terms of the mass defect by:

adding a transpiration source distribution to the body and mean wake surfaces, discretizing the integral equation for the perturbation potential with a low-order panel method, and numerically differentiating the discrete equations.

4.1 Induced Potential with Wall Transpiration

The edge of the boundary layer forms a stream surface in a steady, three-dimensional viscous flow, outside of which the flow is essentially inviscid and irrotational [32]. The presence of the boundary layer displaces the potential flow away from the physical body and is simulated in the VII calculation by adding transpiration sources to the body and wake surfaces.

The integral equation for the perturbation potential with blowing sources is

$$4\pi T\phi(\mathbf{x}) = \iint_{\mathbf{S}_b} (\phi(\xi)\mathbf{n}_\xi \cdot \nabla G(\mathbf{x};\xi) - G(\mathbf{x};\xi)\mathbf{n}_\xi \cdot \nabla\phi(\xi))\, d\xi \qquad (4.1)$$
$$+ \iint_{\mathbf{S}_w} \Delta\phi(\xi)\mathbf{n}_\xi \cdot \nabla G(\mathbf{x};\xi) d\xi + \iint_{\mathbf{S}_b+\mathbf{S}_w} \sigma^v(\xi) G(\mathbf{x};\xi) d\xi$$

where both the potential, ϕ, and the transpiration source strength, σ^v, are unknown. (4.1) is the governing equation for an Equivalent Inviscid Flow (EIF) which extends through the boundary layer to the wall, but includes the velocity perturbation due to boundary-layer growth.

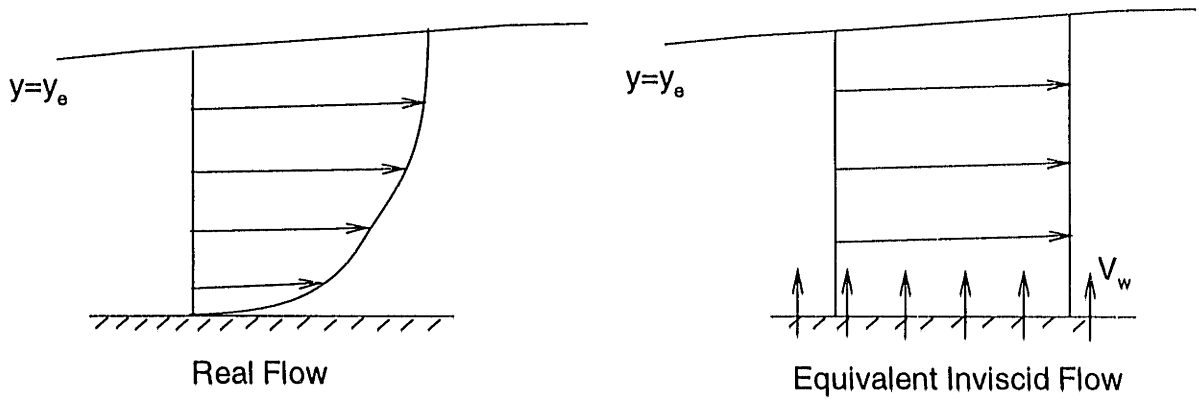

Figure 4-1: Velocity Profiles for Real and Equivalent Inviscid Flows

The transpiration source strength is set so that the velocity normal to the wall in the potential flow is the same as the normal velocity at the edge of boundary layer,

$y = y_e$, in the real viscous flow. The magnitude of the normal velocity at y_e is found by integrating $\frac{\partial v}{\partial y}$ across the boundary layer. Following Nishida [41], we define two components of displacement thickness as

$$\begin{aligned} q_e\delta_x^* &= \int_0^{y_e}(u_e - u)dy \\ q_e\delta_z^* &= \int_0^{y_e}(w_e - w)dy \end{aligned} \tag{4.2}$$

The normal velocity at the edge of the real viscous flow is

$$\begin{aligned} v_e &= \int_0^{y_e}\frac{\partial v}{\partial y}dy \\ &= \int_0^{y_e} -\left(\frac{\partial u}{\partial x} + \frac{\partial w}{\partial z}\right)dy \\ &= \int_0^{y_e}\frac{\partial}{\partial x}(u_e - u)dy + \int_0^{y_e}\frac{\partial}{\partial z}(w_e - w)dy - \int_0^{y_e}\frac{\partial u_e}{\partial x}dy - \int_0^{y_e}\frac{\partial u_e}{\partial x}dy \\ &= \frac{\partial}{\partial x}(q_e\delta_x^*) + \frac{\partial}{\partial z}(q_e\delta_z^*) - y_e\left[\frac{\partial u_e}{\partial x} + \frac{\partial w_e}{\partial z}\right] \end{aligned} \tag{4.3}$$

where the continuity equation has been used to obtain an expression for $\frac{\partial v}{\partial y}$ in terms of u and w as an intermediate step. The partial derivatives can be taken outside the first two integrals in the third line of (4.3) because $(u_e - u)$ and $(w_e - w)$ vanish at the upper limit of integration. An expression for the normal velocity in the EIF is found the same way, with the approximation that the edge velocities u_e and w_e are constant through a distance y_e from the boundary.

$$\begin{aligned} v_e &= V_w + \int_0^{y_e}\frac{\partial v}{\partial y}dy \\ &= V_w - y_e\left[\frac{\partial u_e}{\partial x} + \frac{\partial w_e}{\partial z}\right] \end{aligned} \tag{4.4}$$

Equating (4.3) and (4.4),

$$\sigma^v = \frac{\partial}{\partial x}(q_e\delta_x^*) + \frac{\partial}{\partial z}(q_e\delta_z^*) = \nabla_S \cdot \mathbf{m} \tag{4.5}$$

where the source strength, σ^v, has been substituted for V_w and $\nabla_S \cdot \mathbf{m}$ is the divergence of the mass defect in the local (x,z) surface coordinate system.

4.2 Discrete Equations with Transpiration

The perturbation potential can be decomposed into an inviscid part and viscous correction,

$$\phi = \phi^{(I)} + \phi^{(V)} \tag{4.6}$$

where the inviscid component, $\phi^{(I)}$, is given by the solution of (2.13) and the viscous correction is a function of the transpiration source strengths. Separate expressions for the viscous correction are developed for panels located on the body and in the wake in the following sections.

4.2.1 On-body points

If (4.1) is discretized using the low order panel method described in §2.2.2, the formal solution for the perturbation potential at the i^{th} body collocation point is obtained by inverting the dipole matrix A.

$$\phi_i = \sum_{j=1}^{N_p} A_{ij}^{-1} \left[\sum_{k=1}^{N_p} B_{jk} \left(\frac{\partial \phi}{\partial n} \right)_k - \sum_{m=1}^{M} W_{jm} (\mathbf{U}_\infty \cdot \mathbf{r}_{te})_m \right] + \sum_{l=1}^{N_{tot}} \sum_{k=1}^{N_p} \left[A_{ik}^{-1} B_{kl} \right] \sigma_l^v \quad (4.7)$$

where the first group of terms on the right hand side is the inviscid solution,

$$\phi_i^{(I)} = \sum_{j=1}^{N_p} A_{ij}^{-1} \left[\sum_{k=1}^{N_p} B_{jk} \left(\frac{\partial \phi}{\partial n} \right)_k - \sum_{m=1}^{M} W_{jm} (\mathbf{U}_\infty \cdot \mathbf{r}_{te})_m \right] \quad (4.8)$$

and the second group is the viscous correction,

$$\phi_i^{(V)} = \sum_{l=1}^{N_{tot}} \sum_{k=1}^{N_p} \left[A_{ik}^{-1} B_{kl} \right] \sigma_l^v \quad (4.9)$$

B_{kl} is (k,l) entry of the transpiration source influence coefficient matrix, N_p is the number of panels on the body, and N_{tot} is the total number of panels on the body and wake surfaces.

The inviscid component of (4.7) is readily calculated by LU decomposing the dipole matrix and backsubstituting the known right hand side vector,

$$RHS_j = \sum_{k=1}^{N_p} B_{jk} \left(\frac{\partial \phi}{\partial n} \right)_k - \sum_{m=1}^{M} W_{jm} (\mathbf{U}_\infty \cdot \mathbf{r}_{te})_m \quad (4.10)$$

However, the viscous correction must be left in terms of the unknown transpiration source strengths. (4.9) simplifies to

$$\phi_i = \phi_i^{(I)} + \sum_{l=1}^{N_{tot}} H_{il} \sigma_l^v \quad (4.11)$$

where the product $H = A^{-1}B$ defines an influence coefficient. H is computed by solving N_{tot} linear systems of equations, using the columns of the transpiration source influence matrix B [43] as the right hand side vectors. Each column of H represents

the potential at the N_p body panels due to a unit source at panel l which satisfies the assumption of an undisturbed inflow inside of the body. H depends on the discretization of the body and wake geometries, but is independent of the inflow.

4.2.2 Off-body Points

The induced potential at a wake panel is given by the discrete form of (4.1) with T = 1,

$$\tilde{\phi}_i = \sum_{j=1}^{N_p} \left[\tilde{A}_{ij}\phi_j - \tilde{B}_{ij}(\frac{\partial \phi}{\partial n})_j \right] + \sum_{l=1}^{N_{tot}} \tilde{B}_{il}\sigma_l^v \tag{4.12}$$

where $\tilde{A}_{ij}$ and $\tilde{B}_{ij}$ are the influence coefficients for the potential induced at the i^{th} wake panel due to the j^{th} body dipole and source panels.[1] The wake integral, included in $\tilde{A}$ via the Morino condition, is evaluated as a Cauchy integral so $\tilde{\phi}_i$ represents the average of the potentials on the two sides of the wake. ϕ_j and $(\frac{\partial \phi}{\partial n})_j$ are the strengths of the j^{th} body dipole and source panels.

The inviscid component of the induced potential at wake panel i is

$$\tilde{\phi}_i^{(I)} = \sum_{j=1}^{N_p} \left[\tilde{A}_{ij}\phi_j^{(I)} - \tilde{B}_{ij}(\frac{\partial \phi}{\partial n})_j \right] \tag{4.13}$$

with $\phi_j^{(I)}$ defined by (4.8). The viscous correction includes the direct contribution from the transpiration sources plus an indirect contribution from the body dipoles. The latter is required because the strengths of the body dipole panels are modified by the blowing sources.

$$\tilde{\phi}_i^{(V)} = \sum_{l=1}^{N_{tot}} \left[\sum_{k=1}^{N_p} \tilde{A}_{ik}H_{kl} + \tilde{B}_{il} \right] \sigma_l^v = \sum_{l=1}^{N_{tot}} \tilde{H}_{il}\sigma_l^v \tag{4.14}$$

The first term in square brackets is due to the change in the strength of the body dipole panels caused by the transpiration sources and the second term is the direct contribution from the blowing sources.

[1] The tilde overbar is used to denote that the field point is located on the wake.

4.3 Perturbation Velocities Including Wall Transpiration

4.3.1 In Terms of Source Strength

Perturbation velocities are calculated at the panel nodes by differentiating the induced potential with respect to the surface coordinates x and z,

$$\mathbf{u}_e = \nabla_S \phi \tag{4.15}$$

At the i^{th} node, the velocities are

$$\mathbf{u}_{ei} = \mathbf{u}_{ei}^{(I)} + \nabla_S \left(\sum_{l=1}^{N_{tot}} H_{il} \sigma_l^v \right) \tag{4.16}$$

where $\mathbf{u}_{ei}^{(I)}$ are known inviscid velocities, computed using the algorithm described in §2.3, and the remaining terms are velocities induced by the transpiration sources. Note that $\tilde{H}$ replaces H for a field point on the wake. The potential induced by each transpiration source may be numerically differentiated as well, provided the numerical method takes into account the discontinuity in the derivative at the source panel. By introducing ghost cells, the source-induced velocities can be evaluated properly at boundary nodes.

Two new influence coefficients are defined by taking the surface gradient of the H matrix, $\mathbf{G} = (\frac{\partial H}{\partial x}, \frac{\partial H}{\partial z})$. The elements of these matrices relate the surface velocities at panel nodes to the unit strength transpiration sources.

$$\mathbf{u}_{ei} = \mathbf{u}_{ei}^{(I)} + \sum_{l=1}^{N_{tot}} \mathbf{G}_{il} \sigma_l^v \tag{4.17}$$

4.3.2 In Terms of Mass Defect

The primary boundary layer variables include the mass defect components m_1 and m_2 along the streamwise-crossflow coordinates. Using (4.17) therefore requires that σ_l^v be expressed as a function of m_1 and m_2 via (4.5). However, the streamwise and crossflow directions are unknown until the coupled potential flow/boundary layer problem is solved, so the gradient in (4.5) cannot be easily evaluated along these directions. Instead, the equations are expressed in terms of the mass defect in the surface coordinate system, m_x and m_z, which are related to m_1 and m_2 through vector rotation identities given in Appendix B. The gradient is the easily taken in the x and z directions.

$$\sigma_l^v = (\nabla_S \cdot \mathbf{m})_l$$

where ∇_S and $\mathbf{m}$ are now expressed in x and z coordinates. The panel source strength σ_l^v can be approximated in terms of the nodal values of m_x and m_z by evaluating the surface divergence discretely between the four panel nodes. Specifically, four influence coefficients are assembled by writing the discrete difference formulae in terms of the mass defect at each node, substituting these expressions into (4.17) for σ_l^v, and collecting terms which multiply $\mathbf{m}$ at each node.

The final equations for the edge velocity, expressed in terms of the known inviscid velocity including the inflow, and an unknown viscous correction that is only a function of the mass defect, are

$$u_{ei} = \mathbf{U}_\infty \cdot \hat{e}_x + u_{ei}^{(I)} + \sum_{l=1}^{N_{nodes}} E_{il}^x (m_x)_l + \sum_{l=1}^{N_{nodes}} F_{il}^x (m_z)_l \tag{4.18}$$

$$w_{ei} = \mathbf{U}_\infty \cdot \hat{e}_z + w_{ei}^{(I)} + \sum_{l=1}^{N_{nodes}} E_{il}^z (m_x)_l + \sum_{l=1}^{N_{nodes}} F_{il}^z (m_z)_l \tag{4.19}$$

where N_{nodes} is the total number of panel nodes, $\mathbf{E}_{il} = (E_{il}^x, E_{il}^z)$ are the induced velocities in the x and z directions at node i due to a unit mass defect in the x-direction at node l, and $\mathbf{F}_{il} = (F_{il}^x, F_{il}^z)$ are the induced velocities in the x and z directions at node i due to a unit mass defect in the z-direction at node l. The two summations in these equations represent the perturbation edge velocity due to the boundary layer.

4.3.3 Numerical Validation

E^x is the chordwise component of velocity induced by a chordwise unit mass defect and is analogous to the two-dimensional influence coefficient derived by Hufford [20]. A two-dimensional calculation may be approximated with the current code by introducing high aspect ratio panels, oriented with the longer edge in the spanwise direction.

Figure 4-2 shows E^x for a unit mass defect located near the trailing edge on the upper surface of a wing that is discretized using panels with an aspect ratio of 40. The induced velocities are evaluated along the grid line where the singularity is located and multiplied by 2 to simulate a two-dimensional calculation. The peak on the right hand

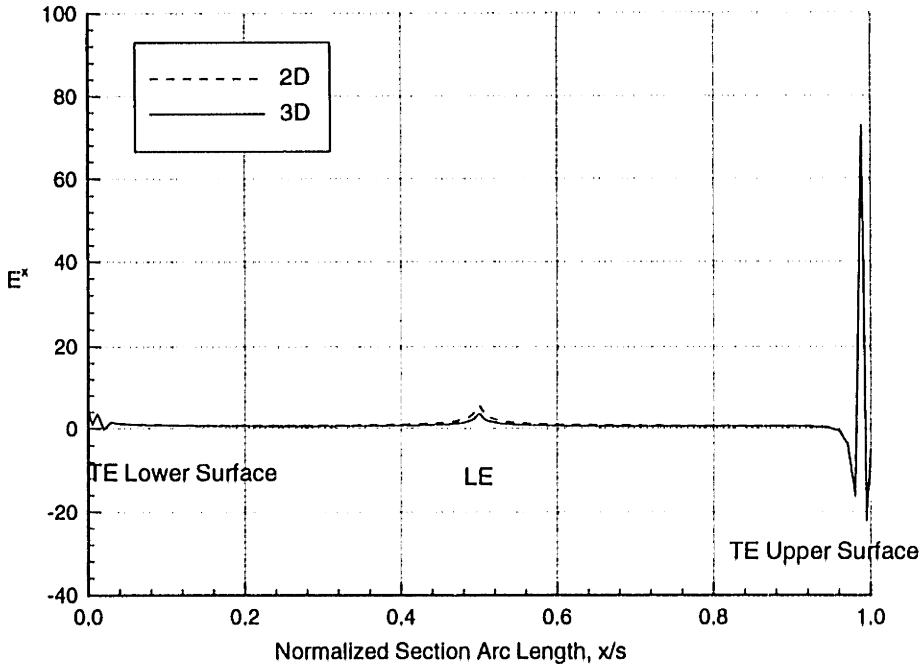

Figure 4-2: Chordwise velocity induced by a unit mass defect in the chordwise direction located on the upper surface near the trailing edge at x/s=0.98

side of the figure shows the strong influence of the singularity on the local velocity. The global influence of the mass defect induces a significant velocity at the leading edge (x/s=0.5) via the Kutta condition and at the trailing edge on the other side of the foil (x/s=0.0). The induced velocity is compared to the two-dimensional influence coefficient computed with a modified version of Hufford's PAN2DBL program [20]. Except for slight differences at the leading edge, the induced velocities computed with two codes are very similar. The difference at the leading edge reflects the unloading due to induced velocities which are present in 3-D but not in 2-D.

The remaining three-dimensional influence coefficients can only be checked against one another. Two comparisons are presented to demonstrate that the mass defect influence coefficients approach the correct limits as panel aspect ratio is varied. Figure 4-3 presents $\mathbf{E}$ and $\mathbf{F}$ for field points on the upper surface of the wing discretized with the high aspect ratio panels. E^z, F^x, and F^z are approximately zero everywhere along the section, demonstrating that influence coefficients for high aspect ratio panels approach the 2-D limit. In practice, the aspect ratio of the panels should not be too large, otherwise the edge velocity equations will not provide strong coupling when the outer flow has a large spanwise component.

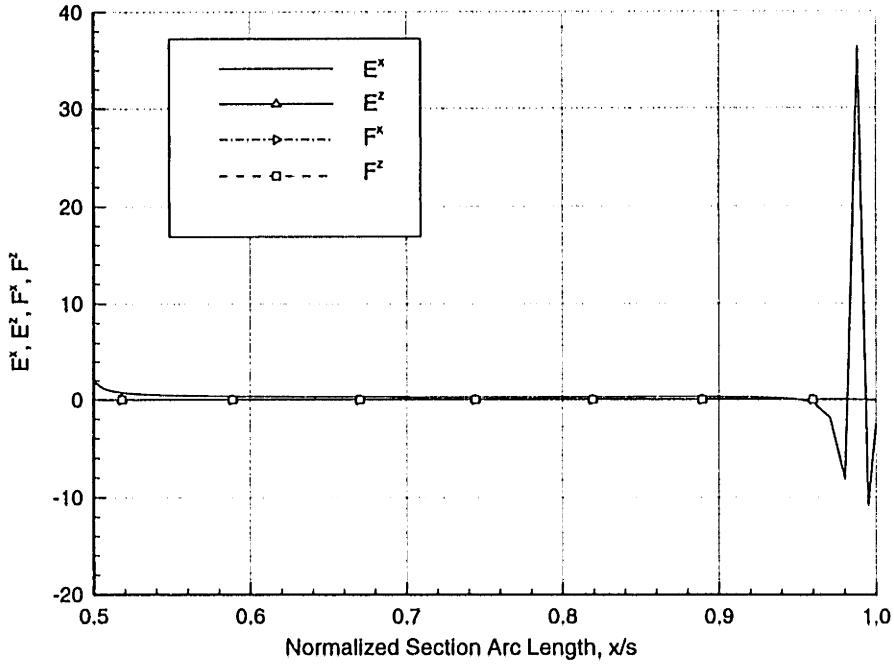

Figure 4-3: Comparison of the **E** and **F** velocity-mass defect influence coefficients for high aspect ratio panels. The induced velocities are evaluated at the nodes of the chordwise grid line where the mass defect is located.

The second comparison is made using influence coefficients computed for a flat wake discretized with square panels. Two mass defect singularities are placed at the center of the surface as shown in Figure 4-4 and the induced velocities evaluated at nodes along the lines A-A and B-B. Figure 4-5 shows the x component of velocity induced by m_x and the z component of velocity induced by m_z. For this example, the velocity fields induced by m_x and m_z are related by a 90^o rotation.

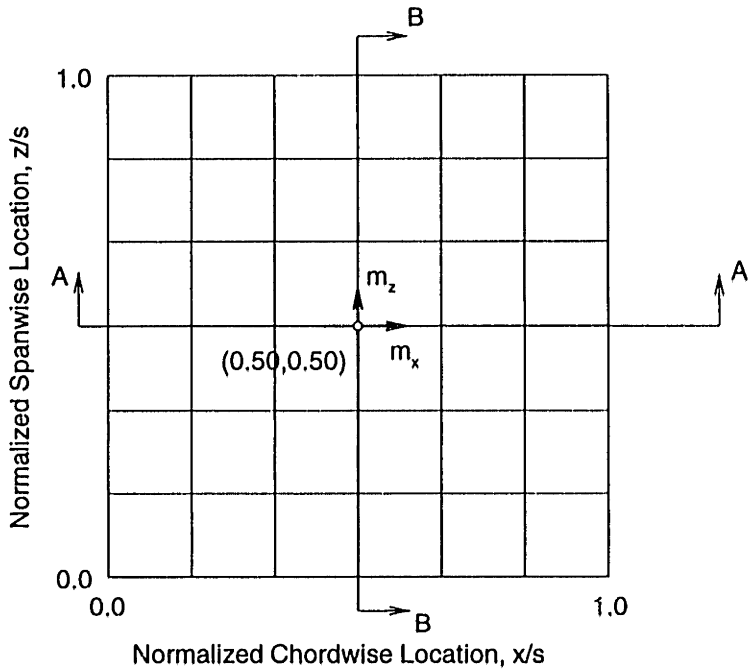

Figure 4-4: Schematic showing location of unit mass defect for a flat geometry discretized with square panels.

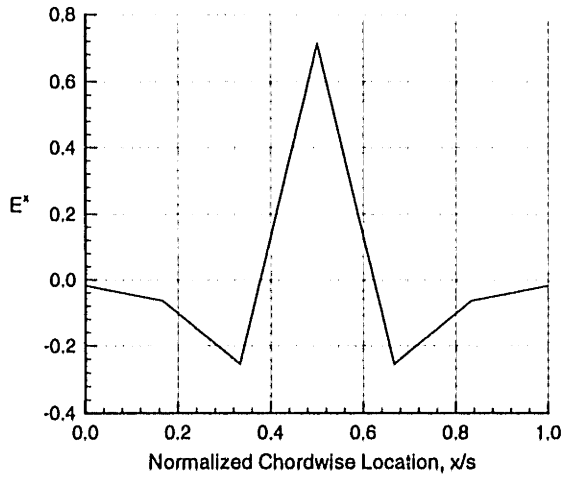

Slice of the velocity field induced by a unit mass defect in the x direction located at (x/s=0.5, z/s=0.5), extracted along the line A-A.

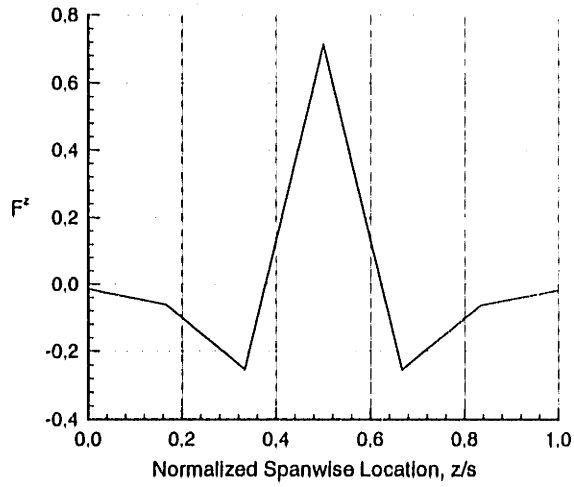

Slice of the velocity field induced by a unit mass defect in the the z direction located at (x/s=0.5, z/s=0.5), extracted along the line B-B.

Figure 4-5: Comparison of the velocity-mass defect influence coefficients for square panels. The spanwise velocity induced by a unit spanwise mass defect is equivalent to the chordwise velocity induced by a unit chordwise mass defect that is rotated 90°.

Chapter 5

Solution of the Coupled Problem

This chapter describes the numerical solution of the coupled boundary layer-potential flow problem which is formulated in the previous chapters. Newton's method is used to solve the non-linear system of boundary-layer equations. The solution procedure differs from other viscous/inviscid interaction schemes because an exact representation of the outer flow is incorporated directly into the system of boundary-layer equations through the Newton Jacobian matrix sensitivities. Furthermore, the equations for all nodes are solved simultaneously.

5.1 Newton's Method for a System of Equations

The solution to a system of equations of the form

$$\mathbf{R}(\mathbf{U}) = 0 \tag{5.1}$$

can be found using Newton's method. If the vector $\mathbf{U}$ at iteration n does not satisfy (5.1), a new solution

$$\mathbf{U}^{n+1} = \mathbf{U}^n + \delta\mathbf{U} \tag{5.2}$$

is determined by linearizing $\mathbf{R}(\mathbf{U}^{n+1})$ about the current solution,

$$\mathbf{R}(\mathbf{U}^{n+1}) = \mathbf{R}(\mathbf{U}^n + \delta\mathbf{U}) \approx \mathbf{R}(\mathbf{U}^n) + \left[\frac{\partial \mathbf{R}}{\partial \mathbf{U}}\right]^n \delta\mathbf{U} = 0, \tag{5.3}$$

and solving a system of equations for the correction $\delta\mathbf{U}$

$$\delta\mathbf{U} = -\left[\frac{\partial \mathbf{R}}{\partial \mathbf{U}}\right]^{n-1} \mathbf{R}(\mathbf{U}^n) \tag{5.4}$$

The iteration is repeated until the correction $\delta\mathbf{U}$ is less than a specified tolerance.

$\left[\frac{\partial \mathbf{R}}{\partial \mathbf{U}}\right]^n$ is the Jacobian matrix evaluated at the i^{th} iteration. Element (i,j) of the matrix is the partial derivative of the i^{th} equation of the residual vector with respect to the j^{th} component of the solution vector. The elements of the Jacobian matrix are computed and the matrix inverted for each iteration.

5.2 System of Equations

In the present application, the system of equations includes the boundary-layer equations, initial conditions, and boundary conditions described in Chapter 3. The computational stencil for an interior node is shown in Figure 5-1. For the weighting function specified in §3.5.2, the residual equations for node i only need to be integrated over the cross-hatched panels. The residual equations at node i depend only on the values of $C_\tau^{1/2}$ and θ_{11} at the nodes marked. However, they are a function of the mass defect at all nodes.

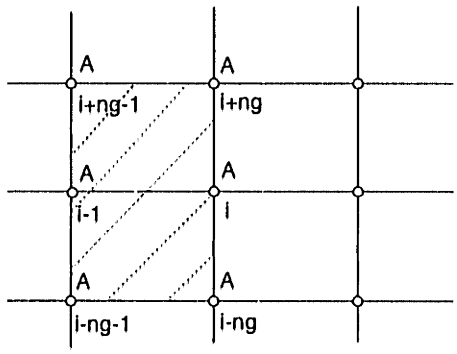

Figure 5-1: Computational grid for node i which is an interior node.

The equations associated with node i are shown symbolically by (5.5).

$$\begin{bmatrix} & & & & & & & & & \\ \ddots & \ddots & & \ddots & \ddots & & \ddots & \ddots & & \\ B & A & A & B & A & A & B & A & A & B \\ & & \ddots & \ddots & & \ddots & \ddots & & \ddots & \ddots \\ & & & & & & & & & \end{bmatrix} \begin{Bmatrix} \delta\mathbf{U}_1 \\ \vdots \\ \delta\mathbf{U}_i \\ \vdots \\ \delta\mathbf{U}_N \end{Bmatrix} = - \begin{Bmatrix} \mathbf{R}_1 \\ \vdots \\ \mathbf{R}_i \\ \vdots \\ \mathbf{R}_N \end{Bmatrix} \quad (5.5)$$

The residual vector $\mathbf{R}_i$ includes the four boundary-layer residual equations for node

i.

$$\mathbf{R}_i^T = \{R_{C_\tau^{1/2}}, R_{k.e.}, R_{x-mom}, R_{z-mom}\}_i^T = \{R_1, R_2, R_3, R_4\}_i^T \tag{5.6}$$

To simplify notation, the components of $\mathbf{R}_i$ are numbered 1-4 as shown. The global residual vector $\mathbf{R}$ is composed of all the nodal residual vectors. The vector of unknowns, $\delta\mathbf{U}_i$, contain the variations in the solution variables at node i.

$$\delta\mathbf{U}_i^T = \{\delta C_\tau^{1/2}, \delta\theta_{11}, \delta m_1, \delta m_2\}_i^T, \tag{5.7}$$

A and B are 4x4 block matrices which contain partial derivatives of the residual equations for node i. An A block is a full matrix which contains the partial derivatives of the residual vector at the i^{th} node for all of the solution variables at the j^{th} node.

$$\begin{bmatrix} \frac{\partial R_1}{\partial C_\tau^{1/2}} & \frac{\partial R_1}{\partial \theta_{11}} & \frac{\partial R_1}{\partial m_1} & \frac{\partial R_1}{\partial m_2} \\ \frac{\partial R_2}{\partial C_\tau^{1/2}} & \frac{\partial R_2}{\partial \theta_{11}} & \frac{\partial R_2}{\partial m_1} & \frac{\partial R_2}{\partial m_2} \\ \frac{\partial R_3}{\partial C_\tau^{1/2}} & \frac{\partial R_3}{\partial \theta_{11}} & \frac{\partial R_3}{\partial m_1} & \frac{\partial R_3}{\partial m_2} \\ \frac{\partial R_4}{\partial C_\tau^{1/2}} & \frac{\partial R_4}{\partial \theta_{11}} & \frac{\partial R_4}{\partial m_1} & \frac{\partial R_4}{\partial m_2} \end{bmatrix} \tag{5.8}$$

If node i is in the interior of the computational domain, there is one A block for each of the nodes marked in Figure 5-1. The remaining blocks of i^{th} row of the Jacobian matrix are filled with B matrices which contain only mass defect sensitivities. The B blocks introduce the elliptic influence of the outer flow.

$$\begin{bmatrix} 0 & 0 & \frac{\partial R_1}{\partial m_1} & \frac{\partial R_1}{\partial m_2} \\ 0 & 0 & \frac{\partial R_2}{\partial m_1} & \frac{\partial R_2}{\partial m_2} \\ 0 & 0 & \frac{\partial R_3}{\partial m_1} & \frac{\partial R_3}{\partial m_2} \\ 0 & 0 & \frac{\partial R_4}{\partial m_1} & \frac{\partial R_4}{\partial m_2} \end{bmatrix} \tag{5.9}$$

5.3 Assembling the Newton System

The solution variables for the system of boundary-layer equations were selected to minimize the number of nodal unknowns. However, the residual equations and elements of the Jacobian matrix are more easily evaluated using the edge velocities and displacement thicknesses. Prior to each Newton iteration, the edge velocities are evaluated using (4.18), (4.19), and the current values of the mass defect and stored. The displacement thicknesses are computed from the mass defect and edge velocities as required.

The system of equations is formed by visiting each panel sequentially and adding its contribution to the residual vector and Jacobian matrix. A local x-z coordinate system is set up on the panel as described in §3.3. After the closure formulae are evaluated in streamline-crossflow coordinates, the boundary-layer variables are transformed into the local panel coordinate system using the identities listed in §B.2. Finally, the elemental residual equations (3.17) are integrated over the panel and added to the global residual vector.

The Jacobian matrix contains the partial derivatives of the residual equations with respect to the solution variables. The derivatives are computed by successive applications of the chain rule at the FORTRAN level to simplify the assembly process. The calculation of sensitivities for each node of a panel proceeds as follows.

1. The sensitivities of all streamline-crossflow boundary-layer variables with respect to $C_\tau^{1/2}, \theta_{11}, \delta_1^*, \delta_2^*, u_e$, and w_e are evaluated and stored. Expressions for the sensitivities are obtained by differentiating the closure relations.

2. The sensitivities of all boundary-layer variables in panel x-z coordinates ($\rho_e q_e^2 \theta_{xx}$, $\rho_e q_e^2 \theta_{xz}, \ldots$) with respect to $C_\tau^{1/2}, \theta_{11}, \delta_1^*$, etc. are evaluated and stored. This requires chain rule differentiation of the transformation equations listed in §B.2. The derivatives are evaluated using the current solution and the results of Step 1.

3. The sensitivities relating displacement thicknesses and edge velocities to the streamwise-crossflow components of mass defect (m_1, m_2) are calculated using the expressions that are derived from the panel method influence coefficients in Appendix C. The derivatives of x-z boundary-layer variables with respect to m_1 and m_2 are evaluated by combining the derivatives from Step 2 with the mass defect sensitivities. For example,

$$\frac{\partial()}{\partial m_1} = \frac{\partial()}{\partial \delta_1^*}\frac{\partial \delta_1^*}{\partial m_1} + \frac{\partial()}{\partial \delta_2^*}\frac{\partial \delta_2^*}{\partial m_1} + \frac{\partial()}{\partial u_e}\frac{\partial u_e}{\partial m_1} + \frac{\partial()}{\partial w_e}\frac{\partial w_e}{\partial m_1} \tag{5.10}$$

After all the sensitivities relating the x-z boundary-layer variables to the solution vector are computed and stored, the entries of the Jacobian matrix are calculated by integrating the derivatives of the elemental residual equations over the panel.

A unique feature of the simultaneous coupling scheme described in this thesis is the elliptic dependence that is introduced by the velocity sensitivities. Since the

sensitivities satisfy the Kutta condition, trailing edge separation changes the bound circulation and causes the location of the attachment line to move.

The boundary-layer equations are ill-posed at separation because they do not constrain the growth of the displacement thickness. When the edge velocity is determined as part of the boundary-layer solution, the large self-influence term of the velocity-mass defect influence coefficients (§4.3.2) keeps the Jacobian matrix well-conditioned.

5.4 Special Equations

The boundary-layer residual equations are replaced with special equations at nodes where an initial condition is required. At nodes along the attachment line, the boundary-layer variables are determined by a 2-D Falkner-Skan similarity solution. The solution at the first streamwise node in the wake is set from the solution at the trailing edge of the wing.

5.4.1 Initial Conditions

The following expressions for the streamwise momentum and displacement thicknesses at the attachment line are incorporated directly into the Newton system. The residual equation for the momentum thickness is

$$R_2 = \theta_{11} - 0.38574\sqrt{\frac{\xi}{Re_\infty u_\xi}} \tag{5.11}$$

and for the displacement thickness is

$$R_3 = \frac{m_1}{q_e} - 0.90649\sqrt{\frac{\xi}{Re_\infty u_\xi}} \tag{5.12}$$

at nodes along the attachment line. R_1 and R_4 are defined to drive $C_\tau^{1/2}$ and m_2 at attachment line nodes to zero.

The distance from the attachment line to the node, ξ, is evaluated in the direction normal to the leading edge and assumed to be a constant. u_ξ is the projection of the edge velocity in the direction normal to the leading edge here. It is calculated by rotating the edge velocity about the surface normal by the angle γ,

$$u_\xi = u_e \cos\gamma + w_e \sin\gamma \tag{5.13}$$

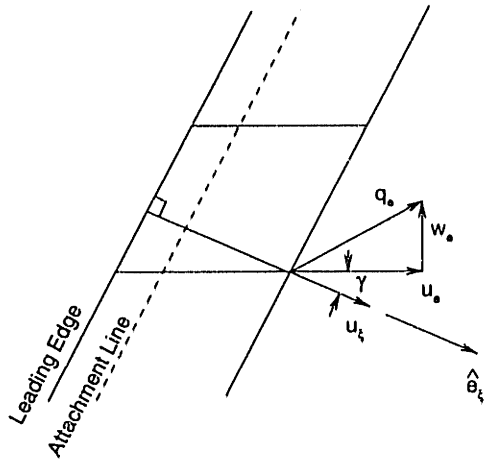

Figure 5-2: Projection of the edge velocity into the ξ direction

with γ defined as the angle between the chordwise and ξ-directed tangent vectors as shown in Figure 5-2.

$$\cos\gamma = \hat{e}_x \cdot \hat{e}_\xi \tag{5.14}$$

The Jacobian-matrix elements for the attachment line equations are found by chain rule differentiation of (5.11) and (5.12) with respect to the solution variables. The sensitivities of u_ξ to the local edge velocities u_e and w_e, required as part of an intermediate calculation, are obtained by differentiating (5.13).

5.4.2 Trailing Edge Equations

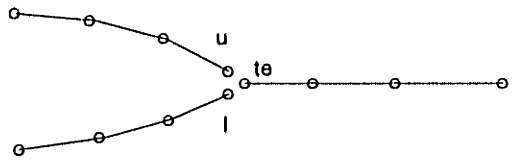

Figure 5-3: Paneling arrangement at section trailing edge.

Figure 5-3 shows the chordwise paneling arrangement near the trailing edge. The first streamwise node in the wake, designated "te", is located at the section trailing edge, as are the nodes marked "u", for upper surface, and "l", for lower surface. Although all three nodes correspond to the same physical point, a separate solution is computed at each one.

The wake is treated as a single viscous layer that convects in the direction of the mean velocity vector. The solution at node "te" provides the initial conditions for the boundary-layer calculations in the wake. The integral boundary-layer equations are replaced with compatibility relations that assign the state vector at node "te" based on the state vectors at nodes "l" and "u". The shear stress coefficient at "te" is the momentum-weighted average of the shear stress coefficients evaluated on the two sides of trailing edge. The remaining terms are simply the sum of the values from the two sides of the trailing edges. The residual equations at the first streamwise node in the wake are:

$$R_1 = C_\tau^{1/2te} - \frac{C_\tau^{1/2u}\theta_{11}^u + C_\tau^{1/2l}\theta_{11}^l}{\theta_{11}^u + \theta_{11}^l} \tag{5.15}$$

$$R_2 = \theta_{11}^{te} - \theta_{11}^u - \theta_{11}^l \tag{5.16}$$

$$R_3 = m_1^{te} - m_1^u - m_1^l \tag{5.17}$$

$$R_4 = m_2^{te} - m_2^u - m_2^l \tag{5.18}$$

The entries of the Jacobian matrix for the trailing edge equations are derived by straightforward differentiation of these equations.

5.5 Numerical Damping

Initial solutions obtained with the coupled boundary-layer solver contained spanwise oscillations in the mass defect distributions near regions of separation. The edge velocity equations should prevent these oscillations, but for the cases presented here, this suppression is weak because the spanwise resolution is coarse. Second order numerical dissipation of the form

$$\nu_2 \delta\eta \frac{\partial^2 m}{\partial \eta^2} \tag{5.19}$$

is added to the x and z momentum equation to damp the oscillations. The η direction is taken along spanwise grid lines and ν_2 is a small number in the range 0.0001-0.001. m is the streamwise mass defect in the x momentum equation and the crossflow mass defect in the z momentum equation. This type of damping is used to control oscillations that occur near shocks in numerical solutions of hyperbolic systems like the Euler equations [16]. Numerical damping stabilizes the numerical solution by increasing the diagonal dominance of the Jacobian matrix.

Second order dissipation can reduce the accuracy of the numerical scheme, but is used as a first approximation here because it is easier to implement than fourth order damping. Two passes over the mesh are required to compute the term proportional to $\frac{\partial^4 m}{\partial \eta^4}$ that is used in the fourth order dissipation formula. Damping will not affect the solution if the mass defect is constant in the direction of the spanwise grid lines.

A numerical experiment was conducted to determine an appropriate value of ν_2 for the problems examined here. Boundary-layer calculations were made for a finite swept wing at an angle of attack of 6.3 degrees. All input parameters and the body and wake discretizatons were held fixed while the value of the damping coefficient was varied from 0.00-0.05. Figure 5-4 shows the streamwise component of the mass defect along the trailing edge on the suction side of the wing for several values of the damping coefficient. The smallest values of ν_2 failed to damp the oscillations while the largest values eliminated any spanwise variation in the solution. Large values also tended to reduce the crossflow through the boundary layer. A value of 0.0005 was found to give results which looked reasonable, without overdamping the solution. The results presented in the next chapter were all calculated with ν_2=0.0005.

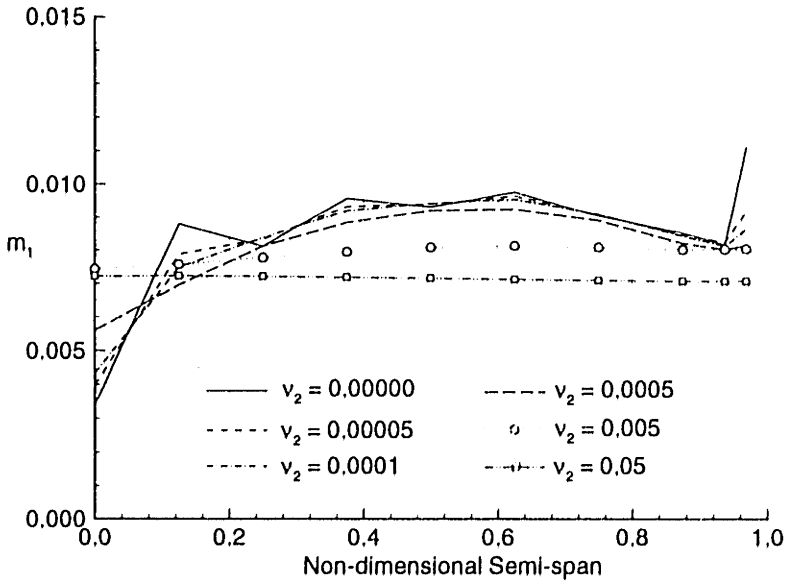

Figure 5-4: Effect of numerical damping coefficient on spanwise distribution of m_1.

The effect of the damping coefficient on the overall solution was checked by comparing the viscous drag coefficients computed from the momentum thickness at the downstream end of the wake sheet for several values of ν_2. The drag values, listed

in Table 5.1, are within 3% of each other although the spanwise distributions of momentum thickness obtained for the various damping coefficients are different.

ν_2	Cd_θ	ν_2	Cd_θ
0.00000	0.007248	0.0005	0.007302
0.00005	0.007459	0.005	0.007280
0.0001	0.007415	0.05	0.007420

Table 5.1: Influence of the damping coefficient ν_2 on the viscous drag coefficient

5.6 Solution of the Linear System

The Jacobian matrix must be inverted once for each Newton iteration. For a typical problem presented in this thesis, the matrix contains approximately 4000-8000 equations and is approximately 50% full due to the global mass influence on the edge velocities. The matrix is currently inverted using a LU decomposition routine that is customized for the DEC Alpha architecture [6]. The CPU time for each Newton iteration (equation assembly, matrix inversion, and solution update) ranges from 2-3 minutes for problems with 600 body panels to approximately 20-25 minutes for problems with 1500 body panels.

The times reported are for a DEC AlphaStation 600 with a processor speed of 256 MHz with the program residing in core memory. The largest problems that are presented here require 384 Mbytes of memory.

The time required to invert the matrix might be reduced if an iterative or custom solver is used. Drela developed a special Gaussian elimination block solver for his 2-D code that speeds up solution of the Newton system [10]. A similar scheme can be developed for the current method, but is not expected to perform as well as the 2-D solver because the 3-D Jacobian matrix is 50% full while the 2-D matrix is only 33% full.

5.7 Solution Update

The standard Newton update may need to be under-relaxed during the first few iterations to prevent the solution from oscillating or even diverging to a non-physical state. An under-relaxation parameter is computed after each Newton step to limit the relative change in the variables $C_\tau^{1/2}, \theta_{11}, \delta_1^*$, and δ_2^* to 60% of their current values.

Clamps are placed on the displacement thicknesses instead of the mass defect to limit the change in the shape parameter [10]. Once relaxed updates of the edge velocities and these variables are calculated, the mass defect is updated using its definition (3.7).

Chapter 6

Numerical Results

This chapter presents numerical results computed using the coupled potential flow/boundary-layer technique described in the previous chapters. The results that are presented include:

- lift and drag coefficient
- chordwise pressure distribution
- chordwise distribution of the integral boundary layer parameters

Calculations are made for three geometries: a highly swept wing, a circular duct, and a two-dimensional airfoil section with trailing edge separation. The predictions are compared to experimental results and other numerical predictions when possible.

6.1 Force Calculations

The lift and drag forces can be computed directly by integrating the pressure and shear stress over the body surface. Surface integration is adequate for lift, but past experience has shown that this approach is inaccurate for drag calculations [48]. A better approach is to apply the momentum theorem and calculate the drag by integrating farfield quantities. This also permits the drag to be separated into viscous and induced components.

The farfield formula for the induced drag requires the potential jump across the wake, however, the potential for the equivalent inviscid flow (EIF) is unknown. The induced drag is estimated using an approximate method that combines the results from pressure integration and the inviscid Trefftz plane calculations. The calculation proceeds as follows:

1. Calculate the lift and induced drag by Trefftz plane integration, using the inviscid spanwise circulation distribution.

2. Compute the inviscid and viscous lift forces using surface integration. The difference between the two is the reduction in lift due to the boundary layer.

3. Subtract the change in lift from the inviscid Trefftz plane lift. If the inviscid lift forces calculated with the two methods are the same, the viscous lift force is just the value obtained by surface integration. This step is included because the inviscid lift forces may be different at large angles of attack if the suction peak is not resolved.

4. Approximate the induced drag for the EIF by

$$D_i^{(v)} = L_v^2 \frac{D_i^{(i)}}{L_i^2} \tag{6.1}$$

where L_v is the viscous lift, L_i is the inviscid lift, and $D_i^{(i)}$ is the inviscid induced drag.

This approximation assumes that the boundary layer does not change the spanwise loading distribution significantly.

The total drag is obtained by adding the induced drag and viscous drag, which is computed by integrating the x-directed momentum defect across the span of the wake at the downstream end.

6.2 RAE 101 Swept Wing

The coupled boundary-layer solver is applied to a 45-degree aft swept wing to demonstrate its full three-dimensional capabilities. The wing had a symmetric RAE 101 section with maximum thickness-chord ratio of 0.12, and was untapered, except at the tip where the leading edge was faired into a lead out tube for the pressure taps [54].

The starboard half of the wing is paneled in the present calculations with the port side represented by a system of images. Although the tip region of the physical model is tapered, the chord and thickness of the computational geometry is kept constant over the entire span. The chordwise distribution of panels is set using a blended spacing algorithm. The spanwise panel distribution is uniform, except at the tip where

the last panel is subdivided to increase the resolution. The entire semi-span of the wing is modeled in the base inviscid solution, however, the outermost panel is excluded from the boundary-layer calculation. Tip panels are dropped from the calculation because the velocity-mass defect influence coefficients cannot be computed properly for nodes along the wing and wake tips. As the mesh is refined in the spanwise direction, the location of the outermost node in the boundary-layer computation approaches the true wing tip.

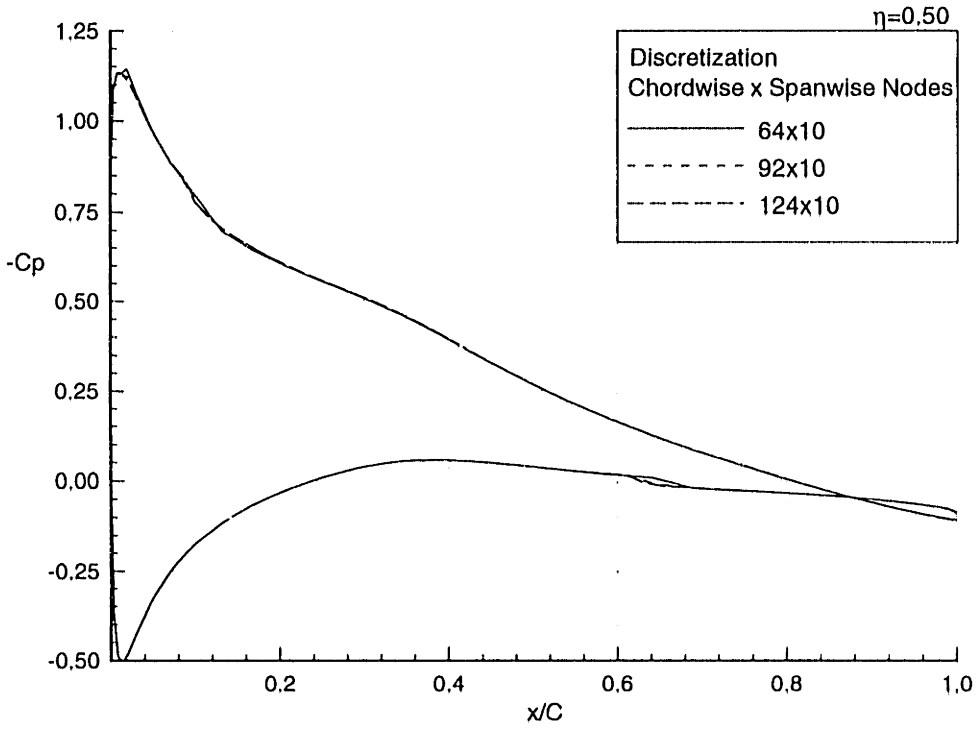

Figure 6-1: Convergence of pressure distribution with the number of chordwise panels.

Calculations are made for several discretizations to investigate the convergence properties of the boundary-layer code. The number of nodes around the airfoil section are varied from 64-124 and the number of nodes across the semi-span from 10-20. Figure 6-1 shows the viscous pressure distribution at the mid-semi-span station, $\eta = 0.50$, for three chordwise discretizations. The calculations are made at an angle of attack of 6.3 degrees and Reynolds number of 2.1×10^6. Small differences between the three predictions are observed at the suction peak and at the transition points (x/c=0.60 on the pressure side, x/c=0.08 on the suction side). The differences at the transition location are caused by the way the transition model is currently im-

plemented: transition is forced at the first node downstream of the specified location, rather than at the location itself. This may be a few percent of the chord from the desired point for coarsely paneled geometries.

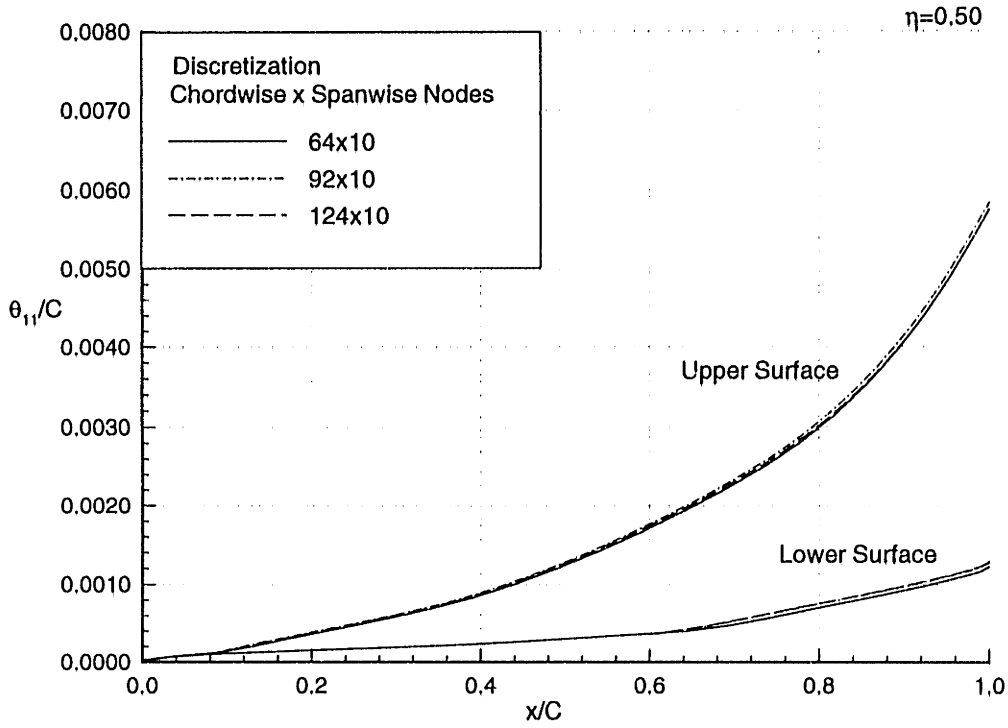

(a) Convergence with the number of nodes around the airfoil section. The momentum thickness at mid semi-span is shown for 64, 92, and 124 chordwise nodes.

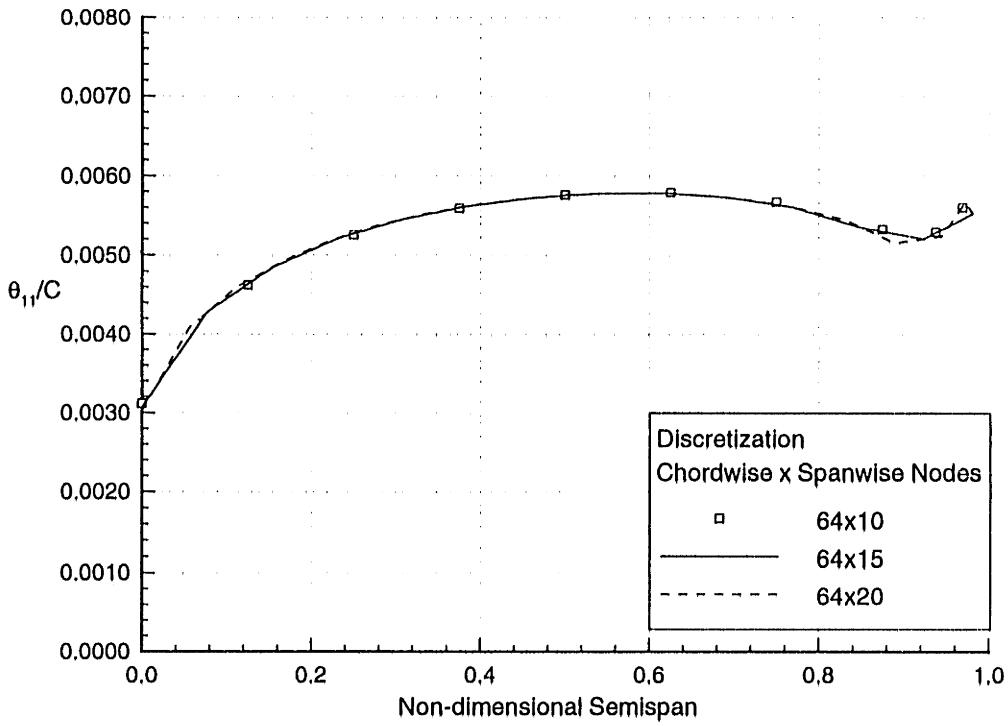

(b) Convergence with the number of spanwise nodes. The momentum thickness at the trailing edge on the suction side of the wing is plotted as a function of the non-dimensional semi-span for 10, 15, and 20 spanwise nodes.

Figure 6-2: Convergence of streamwise momentum thickness with panel number. All calculations are made at $\alpha = 6.3$ degrees

Figure 6-2 shows the convergence of the streamwise momentum thickness with the number of panels for the same operating condition. The upper plot shows the dependence on chordwise node number at $\eta = 0.50$. Here too, the differences between the three discretizations are associated with the transition location. The lower plot shows the dependence on the number of spanwise nodes at the trailing edge on the suction side of the wing. Differences at the tip are believed due to the approximate boundary conditions. The convergence trends for the streamwise momentum thickness are representative of what is observed for the other boundary-layer variables.

Pressure measurements for this wing are reported in [54] for angles of attack from 0-10.7 degrees and a Reynolds number of 1.68×10^6. The measurements were made in a wind tunnel at a Mach number low enough to treat the flow as incompressible. Figure 6-3 shows computed and measured pressure coefficients at three spanwise stations. The inviscid predictions are shown with dashed lines, the viscous predictions with solid lines, and the experimental data with symbols. Boundary-layer computations are made at a Reynolds number of 2.1×10^6 with transition forced at the experimentally-observed locations. The pressure distributions shown for nondimensional span stations $\eta = 0.16$ and $\eta = 0.50$ are for an angle of attack, α, of 6.3 degrees while the one at $\eta = 0.90$ is for an angle of attack of 10.5 degrees. The agreement between the viscous predictions and experimental data is very good, except for the first 20% of the chord at $\eta = 0.90$. The discrepancy at this location is probably related to the simplified representation of the tip in the numerical model.

Integral thicknesses are displayed in Figure 6-4 for span stations $\eta = 0.50$ and $\eta = 0.80$ on the suction side of the wing at $\alpha = 6.3^o$ and a Reynolds number of 2.1×10^6. Computed values are shown as solid lines and experimental thicknesses, obtained by numerically integrating the boundary-layer velocity profiles measured by Brebner and Wyatt [2], are shown as symbols. The crossflow displacement thickness δ_2^* is negative because the crossflow velocity, which is directed outward toward the tip, is positive in the upper surface coordinate system. The agreement between the predicted and experimental values is reasonable, and similar to what Nishida achieved with his boundary-layer solver [41]. However, the current method over-predicts the experimental values while Nishida's method under-predicts them. The current method does appear to do a better job of predicting the crossflow displacement thickness.

Figure 6-5 shows the computed lift and drag coefficients compared with experiment

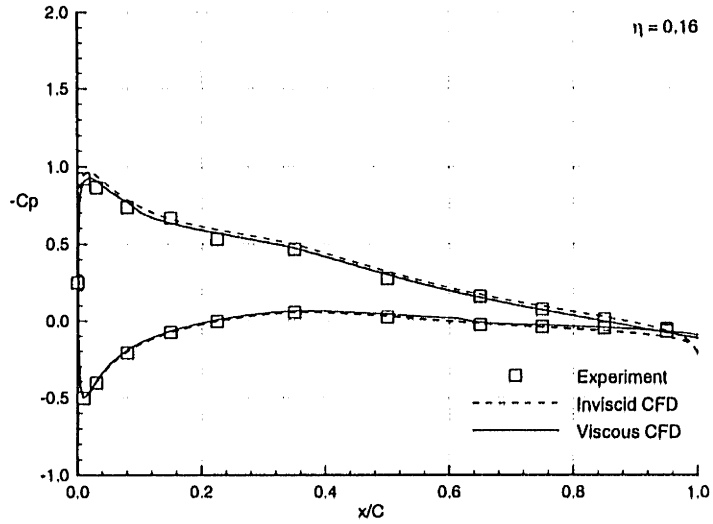

(a) α = 6.3 deg; 16 % semi-span

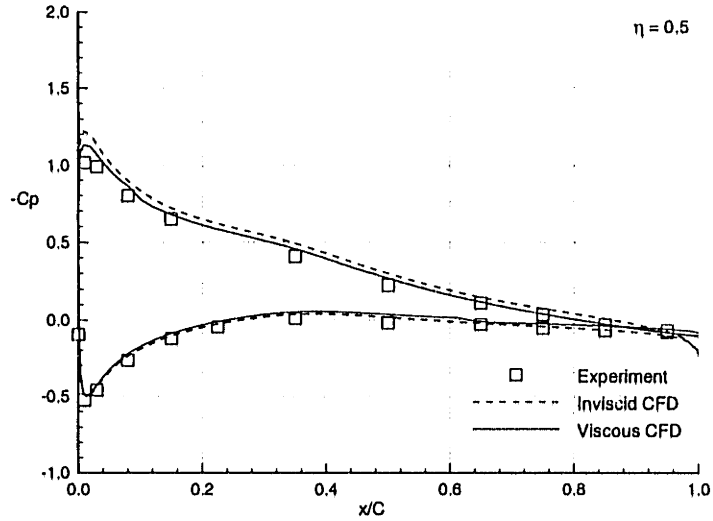

(b) α = 6.3 deg; 50 % semi-span

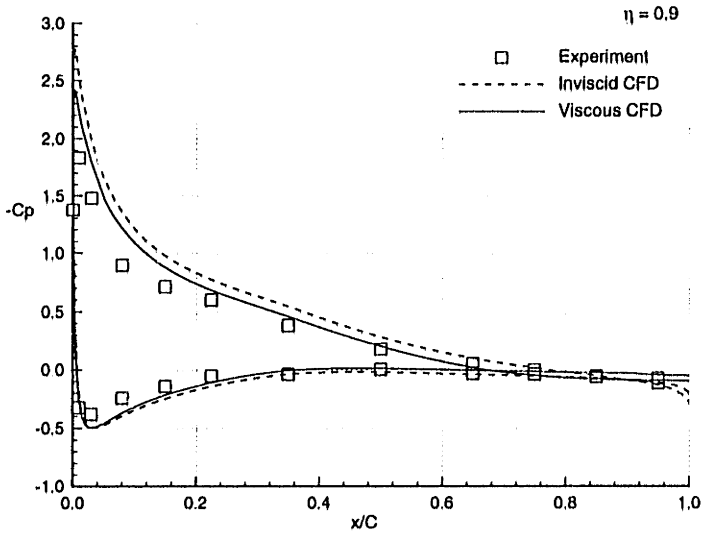

(c) α = 10.5 deg; 90 % semi-span

Figure 6-3: Comparison of calculated and experimental pressure distributions for the RAE 101 swept wing.

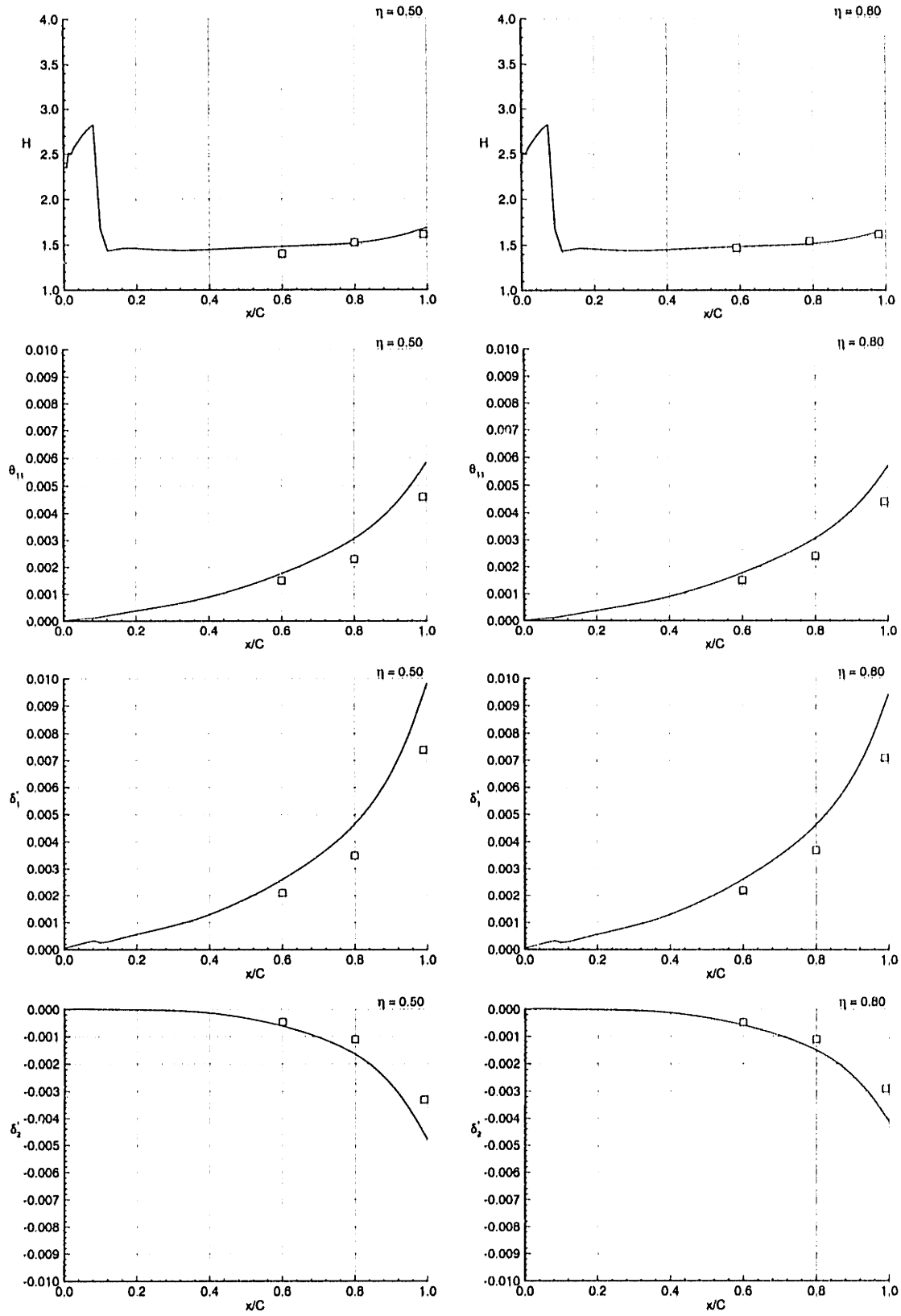

Figure 6-4: Upper surface boundary layer quantities at $\eta = 0.50$ and $\eta = 0.80$ for the RAE 101 swept wing. The operating condition is $\alpha = 6.3°$ at a Reynolds number of 2.1×10^6. Experimental data are shown as symbols and predictions as solid lines. H is the shape factor, θ_{11} and δ_1^* are the streamwise components of momentum and displacement thickness, and δ_2^* is crossflow component of displacement thickness. The integral thicknesses are non-dimensionalized by the wing chord.

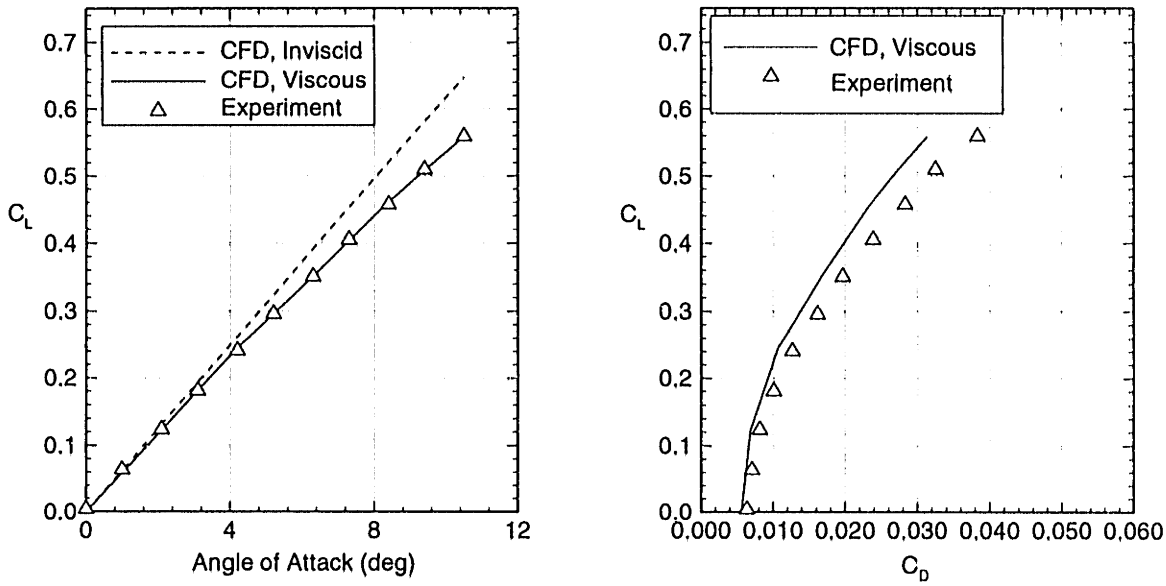

a) CL vs. α b) CL vs. CD

Figure 6-5: Lift and Drag for RAE 45-degree swept wing.

data. The inviscid lift curve is plotted as the dashed line, the viscous lift curve as the solid line, and the experimental data as symbols in the plot of lift vs. angle of attack. Viscous effects are responsible for a reduction in lift of approximately 20% at the largest angles of attack shown. The drag polar compares the lift and drag calculated using the procedure described in §6.1 to the measured data. Lift and drag are also compared to Nishida's farfield predictions in Figure 6-6.

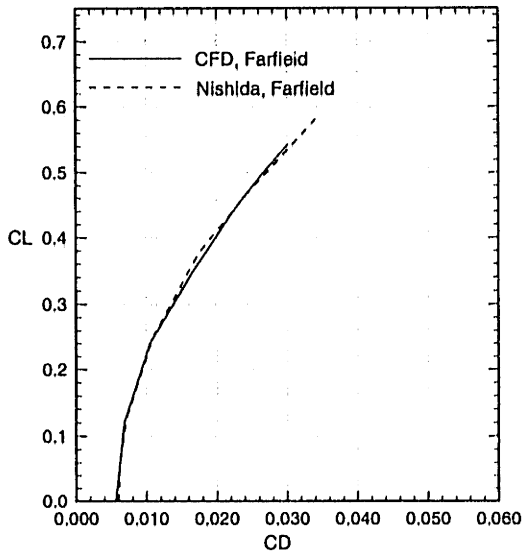

Figure 6-6: Comparison of farfield drag computed with the current model and Nishida's boundary-layer solver.

One objective of this thesis is to develop a numerical method that is capable of predicting three-dimensional separation. Figure 6-7 shows the streamlines predicted for the suction side of the wing at $\alpha = 10.5^o$. The inflow is from left to right, with midspan of the wing located at the lower, left side of each plot. Although the outer flow over the wing is essentially aligned with the inflow, the limiting wall streamlines are directed outward along most of the trailing edge. Convergence of the wall streamlines is three-dimensional flow separation [28].

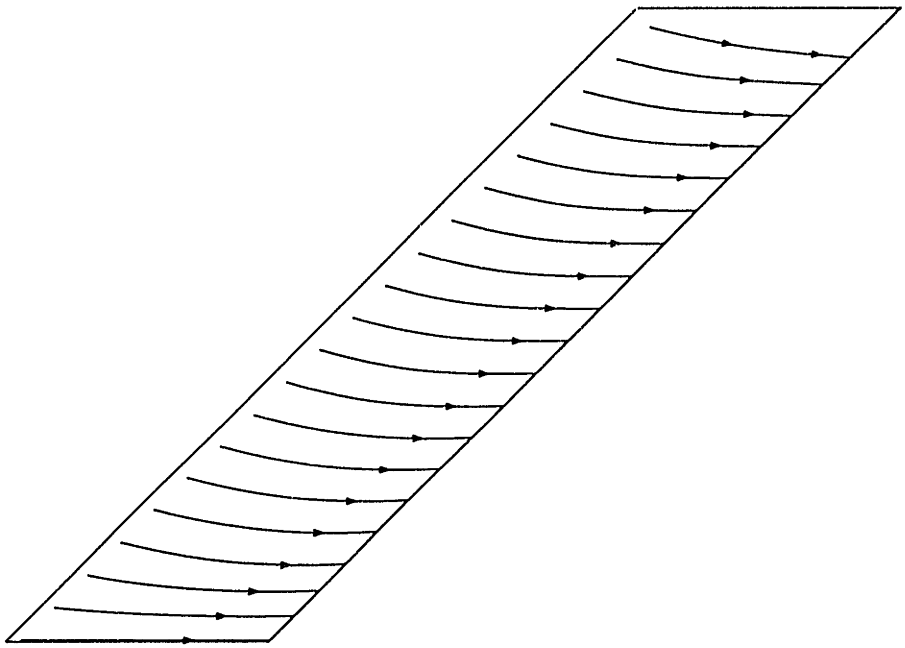

a. Outer flow streamlines.

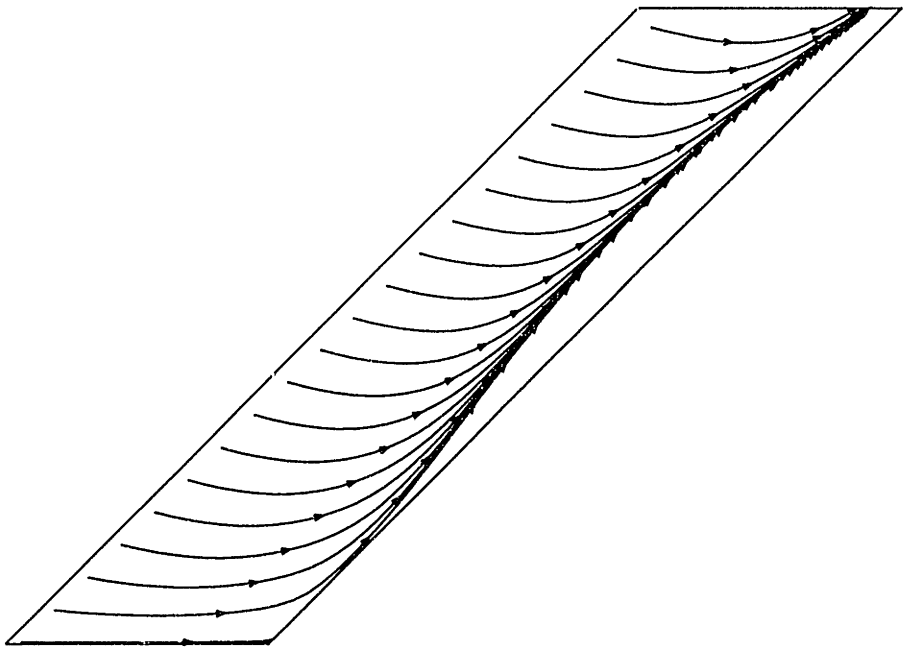

b. Limiting wall streamlines.

Figure 6-7: Streamline traces on the upper surface of the swept wing at $\alpha = 10{,}5^o$. The inflow is from left to right

6.3 DTMB Duct II

DTMB Duct II is representative of a circular duct that might be used in a ducted propulsor. The airfoil section of the duct is a NACA 66 Mod. thickness form with a NACA $a = 0.8$ meanline. The thickness-chord and camber-chord ratios are 0.10 and 0.04 respectively and the chord-diameter ratio for the duct is 0.8. Figure 6-8 shows the paneled duct. The section at the top of the duct is labeled $\phi = 0^o$ and the section at the bottom $\phi = 180^o$. When the duct is pitched, the top section is placed at a positive angle of attack and the bottom section at a negative angle of attack.

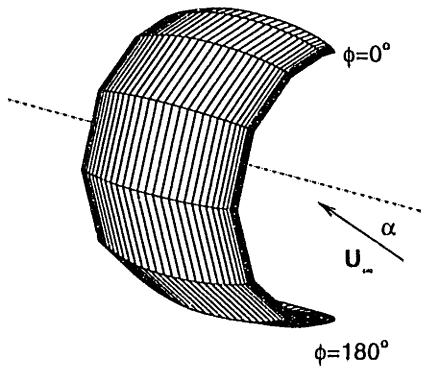

Figure 6-8: Paneled geometry for DTMB Duct II. The top of the duct is at $\phi = 0^o$ and the bottom at $\phi = 180^o$. Only the starboard side of the duct is paneled for the calculation.

Measurements of lift, drag, and pressure coefficient along the inner and outer surfaces of the duct at $\phi = 0^o$ and 180^o were reported by Morgan and Caster for pitch angles of +/-10 degrees [35]. The experiments were conducted with a 20 inch diameter model at a Reynolds number of 2.06×10^6. All experiments were run with natural transition. Our calculations are made with transition forced 5% of the chord aft of the leading edge on both the inner and outer surfaces of the duct at pitch angles of 0^o and 2^o. The transition line is moved forward to x/c=0.01 for larger pitch angles.

The duct is modeled numerically by cubic integral B-splines in the chordwise direction and quadratic rational B-splines in the circumferential direction. The use of rational splines enables an exact representation of the circular cross-section of the duct. The weight and knot vectors and placement of the control net vertices for the circumferential splines are set using values published by Rogers and Adams for conic sections [47]. Longitudinal symmetry of the duct is exploited in the calculations re-

ported here. Only the starboard side of the duct is paneled while the port side is represented by images. Chordwise panels are spaced using the blended spacing algorithm while the circumferential panels are cosine-spaced to cluster panels at the top and bottom of the section. The results presented here are for a discretization with 98 nodes around the airfoil section and 13 nodes along the half circumference.

The chordwise pressure distribution at 0 degree incidence is shown in Figure 6-9. Viscous effects reduce the mass flow through the duct, hence the circulation around the section, and improve the agreement between the predicted and measured pressure distributions. The viscous pressure distribution shows a pressure jump across the trailing edge which is believed to be caused by the inviscid velocity calculation at the trailing edge. Figure 6-10 presents the predicted and experimental pressure distributions for the top and bottom sections with the duct pitched 4^o. The viscous solution is closer to the measured data, although the suction peak at $\phi = 0^o$ is not captured very well.

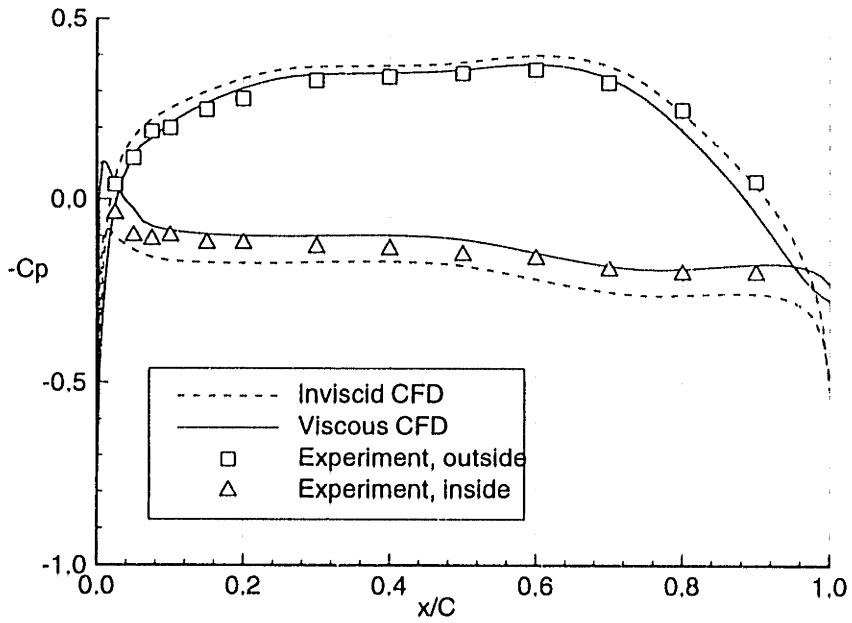

Figure 6-9: Comparison of predicted and measured pressure distributions on DTMB Duct II at 0 deg. incidence.

The computed shape parameter is presented in Figure 6-11 for the duct in the unpitched condition. At the trailing edge on the suction side, the shape parameter exceeds 2.8, indicating turbulent flow separation.

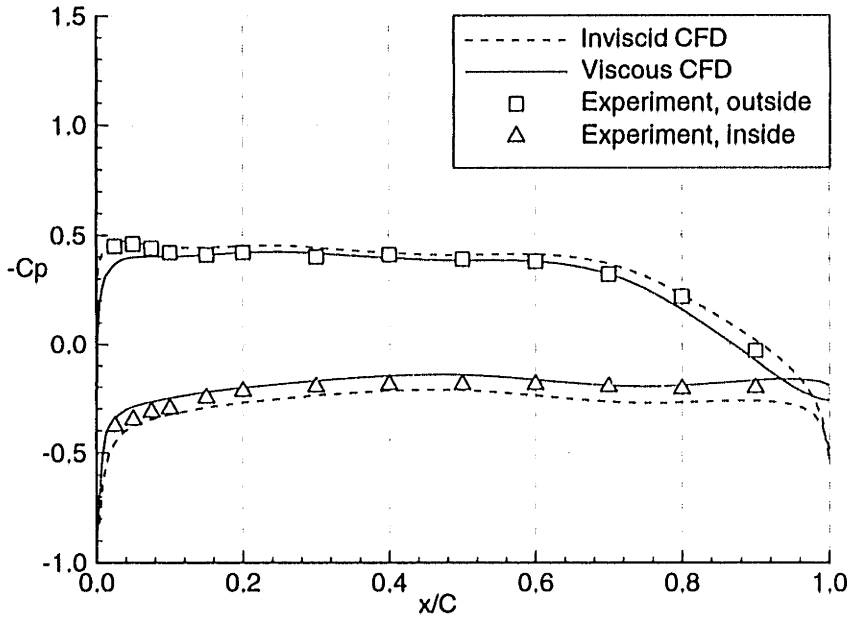

(a) Top section of duct, ($\phi = 0^o$)

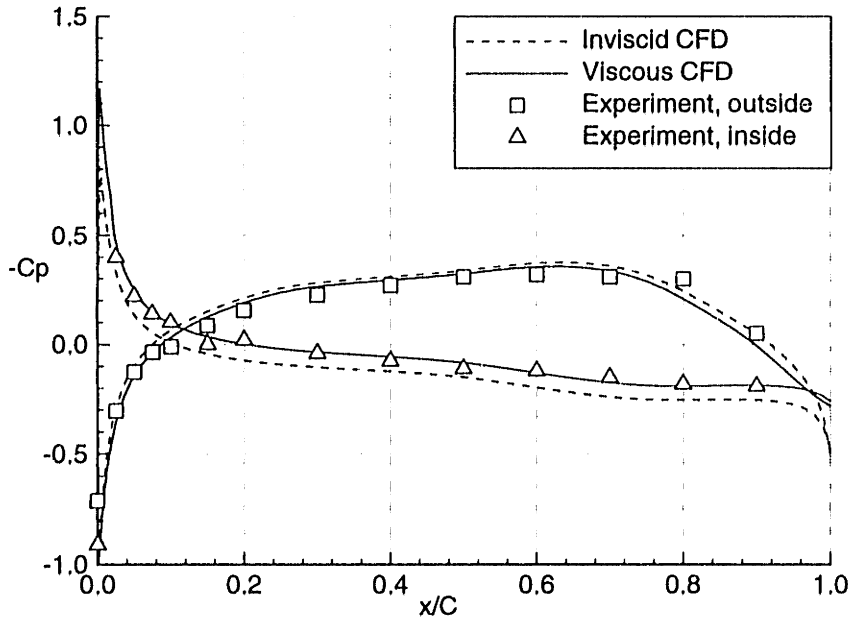

(b) Bottom section of duct, ($\phi = 180^o$)

Figure 6-10: Comparison of predicted and measured pressure distributions on DTMB Duct II, with duct pitched 4 degrees.

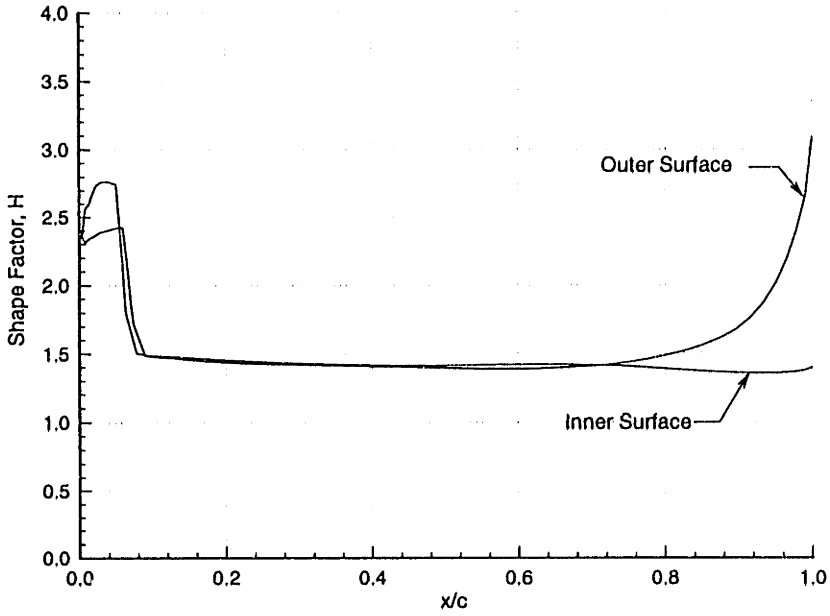

Figure 6-11: Shape parameter for Duct II at 0 degree incidence.

The calculation did not converge for pitch angles greater than 5 degrees for this geometry because laminar separation is predicted on the inside of the duct at $\phi = 180^o$, just downstream of the leading edge. The boundary-layer solver cannot treat laminar separation bubbles properly at this time since it is only configured for fixed transition. Efforts to trip the flow upstream of the separation location did not work either because separation occurred within the first 1% of chord. A short region of laminar flow is required near the attachment line because the boundary layer is modeled using a Falkner-Skan similarity solution. The prediction of a leading edge separation bubble is consistent with the measured pressure distributions for larger pitch angles. Morgan and Caster conclude that there is leading edge separation at a pitch angle of 8^o. However, the lowest pitch angle with separation cannot be determined from the available experimental data.

Figure 6-12 presents lift and drag coefficients for Duct II at angles up to 5 degrees. The coefficients are non-dimensionalized by the mean chord, c, and duct radius, R, at the trailing edge.

$$C_L = \frac{L}{\frac{1}{2}\rho U^2 cR} \qquad C_D = \frac{D}{\frac{1}{2}\rho U^2 cR} \tag{6.2}$$

The inviscid lift curve from the Trefftz plane calculation is shown as the dashed line,

the viscous prediction as the solid line, and the experimental data as symbols. Although the predicted lift matches the experimental data well, the drag is about 25% low. The poor agreement between the predicted and experimental drag is not understood. Drag calculated with an axisymmetric boundary-layer solver for 0^o incidence is similar to the three-dimensional prediction.

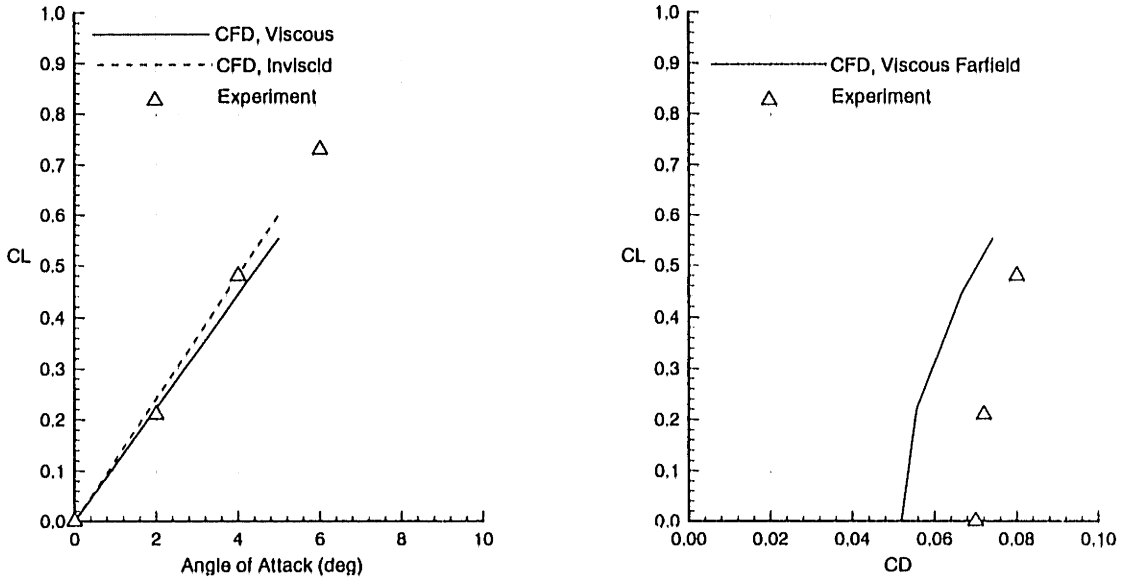

a) CL vs. α b) CL vs. CD

Figure 6-12: Lift and Drag for DTMB Duct II.

6.4 B1 Foil

A two-dimensional section is analyzed to demonstrate the convergence properties of the farfield viscous drag calculation and the ability of the method to predict flows with separation. The B1 hydrofoil, shown in Figure 6-13, was tested in the MIT variable pressure water tunnel as part of a 2-D flapping foil experiment [34]. The section is a NACA 16 thickness form with a thickness-chord ratio of 0.0884 and a NACA a=0.8 meanline with a camber-chord ratio of 0.02576. An anti-singing bevel which is applied to the trailing edge on the suction side causes turbulent separation over the last few percent of the chord. The foil was tested at an angle of attack of 1.2^o and Reynolds number of 3.78×10^6. Boundary layer trips were applied at $x/C = 0.105$ on both sides of the section to induce turbulent flow.

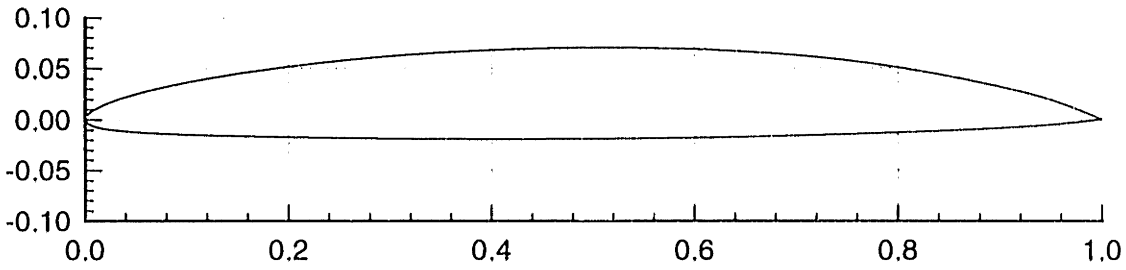

Figure 6-13: B1 Geometry

Two-dimensional calculations are approximated with the current method by analyzing the flow over the midspan section of a high aspect ratio wing. The section of the wing is represented by a single spanwise panel. In the potential flow calculation image panels are placed outboard of the section to extend the wing 40 chords in both directions. Even this is incomplete because the angle of attack must be increased by approximately 2% to match a calculation made with a 2-D panel code. Symmetry boundary conditions are applied along both edges in the boundary-layer calculation.

Although wall-induced flow curvature influences the experimental chordwise load distribution, this effect is not modeled in the present calculations. Calculations are made for the foil in unbounded flow using the experimental Reynolds number and transition location. The angle of attack is increased to match the experimental lift coefficient of 0.466. Two-dimensional RANS calculations with and without tunnel walls were completed by Dannecker for a similar foil [8]. His results indicate that

the walls have a larger effect on the lift than on the development of the boundary layer at the trailing edge of the foil. The current predictions are compared with experimental data even though the problem is modeled in a simplified fashion. Figure 6-14 shows the computed and measured shape parameter, momentum thickness, and displacement thickness for the B1 foil. The agreement between the prediction and data is excellent for all three quantities. Turbulent separation is predicted and was observed at x/c=0.98 on the suction side of the foil.

Figure 6-15 presents the drag predicted with the current method as a function of panel number. For a 2-D problem the drag is simply the viscous component obtained from the farfield momentum thickness. Also shown on the figure is the measured drag and the converged prediction made with Drela's XFOIL boundary-layer solver [10]. The two calculations compare well, but are lower than the experimental drag coefficient of 0.0101. The difference between the predictions and experiments may not be as large as shown because Lurie indicates the experimental drag is probably too high based on the way it is calculated [34].

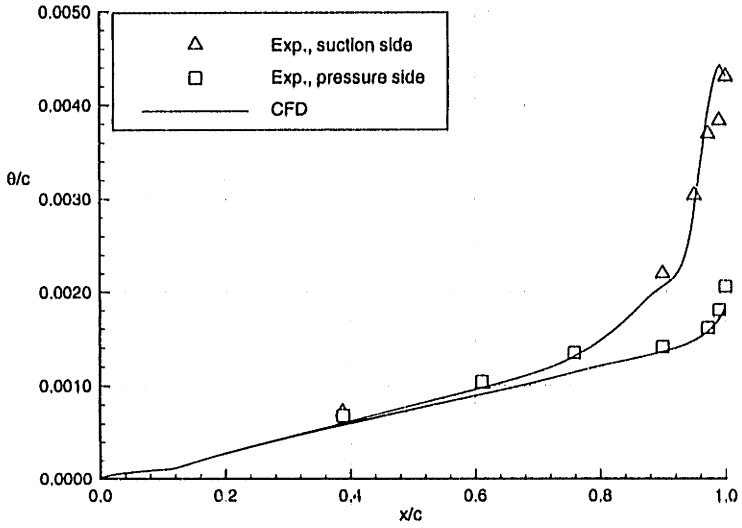

(a) Momentum thickness

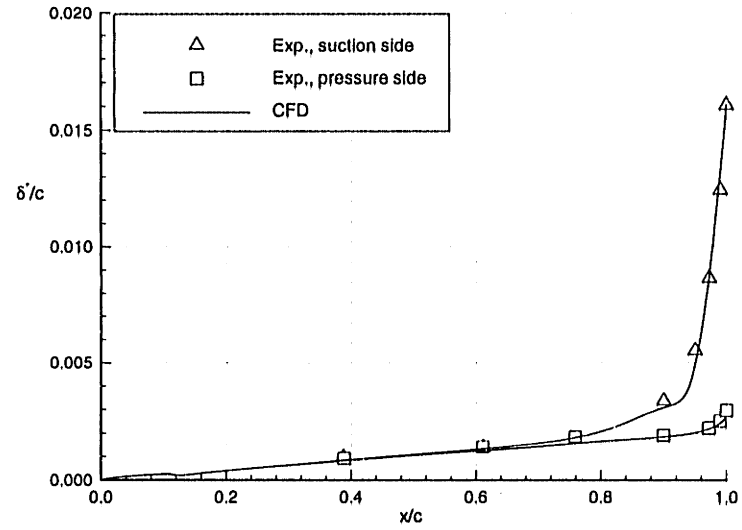

(b) Displacement thickness

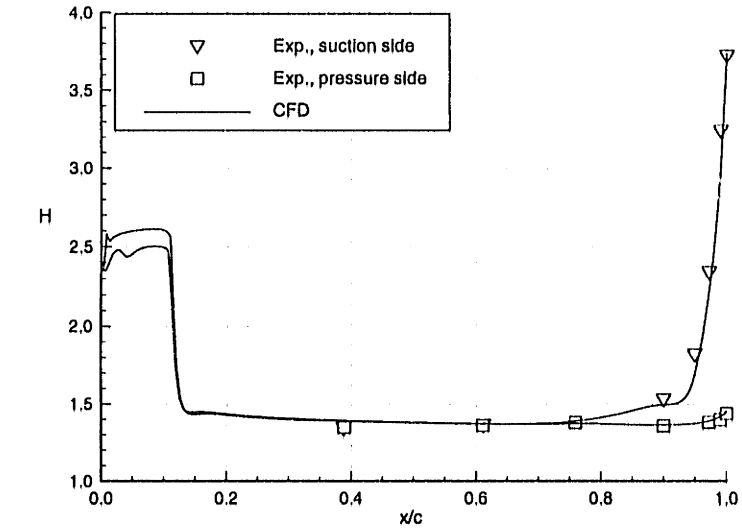

(c) Shape parameter

Figure 6-14: Boundary-layer parameters for B1 foil at $CL_{vis} = 0{,}48$

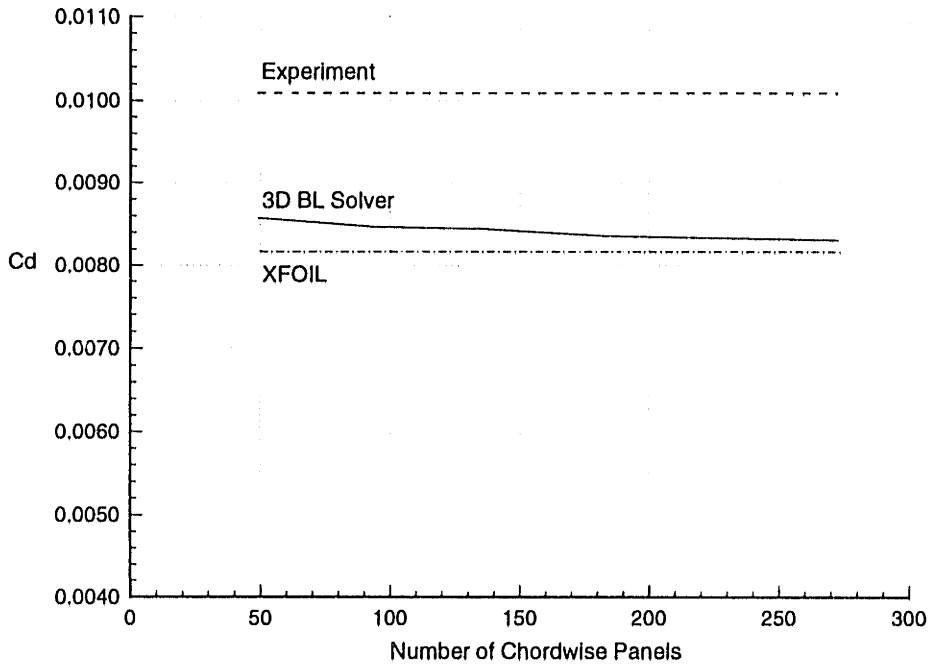

Figure 6-15: Convergence of drag coefficient with chordwise panel number for the B1 foil.

Chapter 7

Conclusions and Recommendations

7.1 Conclusions

7.1.1 Summary of Numerical Implementation

A simultaneous viscous/inviscid interaction (VII) algorithm for the analysis of three-dimensional lifting surface flows is outlined in this thesis. The procedure couples a constant strength panel method and the three-dimensional integral boundary-layer equations by superimposing a source distribution on the body and wake surfaces. The discrete integral equation for the inviscid flow is transformed into equations for the edge velocity which depend only on viscous variables. The boundary layer equations are discretized using the finite element method and solved numerically by a full Newton method. By using the edge velocity equations to close the system of boundary layer equations, an exact inviscid model which satisfies local and global interaction between the inner and outer flows is incorporated in the calculation.

The current formulation uses a surface discretization of the body and inviscid wake sheet, eliminating the difficulties and expense of gridding a three-dimensional flow field as is typically required for a Navier-Stokes solver or other VII methods. The geometries are represented by non-uniform rational B-splines in the panel code, making the method compatible with existing geometric modeling packages. Moreover, the grid metric terms needed to evaluate the edge velocity equations are computed analytically from the B-spline expansion rather than numerically from the coordinates of the surface grid lines.

7.1.2 Performance of the Method

Calculations made for a finite swept wing demonstrate the current method converges as the number of panels is increased in the chordwise and spanwise directions. Relatively few panels are required to obtain a reasonable solution unless localized features of the flow must be resolved.

Comparisons between experimental data and predictions were presented for a 45^o swept wing, an annular wing, and a two-dimensional hydrofoil section. Good agreement in the overall forces, pressure distributions, and boundary layer integral quantities was shown for flows with three-dimensional effects. The algorithm is stable for separated flows where the wall shear stress vanishes as well as for flows with 3-D separation lines.

Numerical smoothing is required to prevent spanwise oscillations when the geometry is not resolved well enough. Dissipation is introduced by adding second order damping to the X and Z momentum equations. The results of a numerical experiment indicate that the damping coefficient should be small, otherwise all spanwise variations in the solution are eliminated. If the spanwise resolution can be increased so the panel aspect ratio is smaller, the edge velocity equations will suppress the oscillations without numerical dissipation.

7.2 Recommendations

Additional research is suggested in the following areas to improve the method presented here.

Iterative Matrix Solution The computational requirements for the solution of the boundary layer problem are large because the Jacobian matrix is currently stored in core memory and inverted using a direct solver. The matrix is $\mathcal{O}(50\%)$ full due to the elliptic influence of the mass defect sensitivities, however many of these sensitivities are small and and can be dropped without affecting the convergence rate of the Newton method significantly [10]. They would all be retained in computing the viscous edge velocity, so that the final solution would be unaffected. By pre-sorting the velocity-mass defect influence coefficients so only significant values are retained, it may be possible to implement an iterative sparse matrix solver in the boundary

layer code. This modification is expected to reduce the memory requirements, speed up the assembly of the Jacobian matrix, and reduce the time required to invert the matrix during each Newton step. As a result, it would improve the performance of the method significantly as well as permit the analysis of more complex geometries.

Trailing Edge Loading The computed pressure distributions for cambered airfoil sections show finite trailing edge loading. This is believed to be caused by the algorithm used to compute the "inviscid" component of the velocity at trailing edge nodes, but should be examined more closely to determine the actual source of the problem.

Wake Modeling The wake geometry is presently linearized and assumed to follow the nose-tail line of the airfoil section. However, previous studies [44, 46] indicate that wake alignment can have an effect on the inviscid solution for a swept wing, especially near the tip. It is important that the panel code incorporates features which improve the inviscid prediction since it provides the base solution for the coupled problem. A wake-tracing model should be added to the inviscid code.

Bibliography

[1] F. Arnold and F. Thiele. Laplace Interaction Law for the Computation of Viscous Airfoil Flows in Low- and High-speed Aerodynamics. *AIAA Journal*, 31(11):2178–2185, November 1994.

[2] G.G. Brebner and L.A. Wyatt. Boundary Layer Measurements at Low Speed on Two Wings of 45^o and 55^o Wweep. CP 554, Aeronautical Research Council, 1961.

[3] D. Catherall and K. W. Mangler. The Integration of the Two-Dimensional Laminar Boundary-Layer Equations Past the Point of Vanishing Skin Friction. *Journal of Fluid Mechanics*, 26:163–182, 1966.

[4] T. Cebeci, D. Sedlock, K. C. Chang, and R. W. Clark. Analysis of Wings With Flow Separation. *Journal of Aircraft*, 26(3):214–220, 1989.

[5] W. Coney. Some Notes on the Calculation of Viscous Effects on Lift. Technical Report 89-8, Department of Ocean Engineering, Massachusetts Institute of Technology, 1989.

[6] Digital Equipment Corporation. DXML Extended Math Library.

[7] J. Cousteix. Three-Dimensional and Unsteady Boundary Layer Computations. *Annual Review of Fluid Mechanics*, 18:173–196, 1986.

[8] J. D. Dannecker. A Numerical Study of Fluid Flow Around Two-Dimensional Lifting Surfaces. Master's thesis, Massachusetts Institute of Technology, June 1997.

[9] M. Drela. *Two-dimensional Transonic Aerodynamic Design and Analysis Using the Euler Equations.* PhD thesis, Department of Aeronautics and Astronautics, Massachusetts Institute of Technology, December 1985.

[10] M. Drela. XFOIL: An Analysis and Design System for Low Reynolds Number Airfoils. In T. J. Mueller, editor, *Low Reynolds Number Aerodynamics*. Springer-Verlag, June 1989.

[11] M. Drela. Private communication, February 1997.

[12] J. Green, D. Weeks, and J Brooman. Prediction of Turbulent Boundary Layer and Wakes in Compressible Flow By a Lag-Entrainment Method. R. & M 3791, Aeronautical Research Council, 1977.

[13] N. C. Groves. An Integral Prediction Method for Three-Dimensional Turbulent Boundary Layers on Rotating Blades. In *Proceedings of the Propellers '81 Symposium*, Virginia Beach, VA, September 1981. SNAME.

[14] N. C. Groves and M.S. Chang. A Differential Method for Three-dimensional Laminar and Turbulent Boundary Layers of Rotating Blades. In *Proceedings of the* 15^{th} *ONR Symposium on Naval Hydrodynamics*, Hamburg, Germany, 1984.

[15] C. Hirsch. *Numerical Computation of Internal and External Flows, Vol. 1: Fundamentals of Numerical Discretization.* John Wiley and Sons., New York, 1992.

[16] C. Hirsch. *Numerical Computation of Internal and External Flows, Vol. 2: Computational Methods for Inviscid and Viscous Flows.* John Wiley and Sons., New York, 1992.

[17] C. Y. Hsin. *Development and Analysis of Panel Methods for Propellers in Unsteady Flow.* PhD thesis, Department of Ocean Engineering, Massachusetts Institute of Technology, September 1990.

[18] C. Y. Hsin, J.E. Kerwin, and S.A. Kinnas. A Panel Method for the Analysis of the Flow Around Highly Skewed Propellers. In *Proceedings of the Propellers/Shafting '91 Symposium*, Virginia Beach, VA, September 1991. SNAME.

[19] K. H. Huebner, E. A. Thornton, and T. G. Byron. *The Finite Element Method for Engineers.* John Wiley & Sons, New York, 1995.

[20] G. S. Hufford. Viscous Flow Around Marine Propellers Using Boundary Layer Strip Theory. Master's thesis, Department of Aeronautics and Astronautics, Massachusetts Institute of Technology, June 1992.

[21] B. Hunt. The Mathematical Basis and Numerical Principles of the Boundary Integral Method for Incompressible Potential Flow Over 3-D Aerodynamic Configurations. In B. Hunt, editor, *Numerical Methods in Applied Fluid Dynamics*, pages 39–135. Academic Press, New York, 1980.

[22] J. P. Johnston. *Three-dimensional Turbulent Boundary Layers.* PhD thesis, Gas Turbine Laboratory, Massachusetts Institute of Technology, 1957.

[23] J. E. Kerwin, D. P. Keenan, S. D. Black, and J. G. Diggs. A Coupled Viscous/Potential Flow Design Method for Wake-Adapted, Multi-stage, Ducted Propulsors. In *Proceedings, Society of Naval Architects and Marine Engineers*, 1994.

[24] J.E. Kerwin, S.A. Kinnas, J.-T. Lee, and W.-Z. Shih. A Surface Panel Method for the Hydrodynamic Analysis of Ducted Propellers. *Trans. SNAME*, 95, 1987.

[25] S.A. Kinnas, S. Mishima, and W.H. Brewer. Nonlinear Analysis of Viscous Flow Around Cavitating Hydrofoils. In *Twentieth Symposium on Naval Hydrodynamics*, pages 717–737, Washington, D.C., 1996. National Academy Press.

[26] S.A. Kinnas, S. Pyo, C. Y. Hsin, and J.E. Kerwin. Numerical Modeling of Propeller Tip Flows. In *Proceedings of the Sixth International Conference on Numerical Ship Hydrodynamics*, 1993.

[27] V.E. Kovalev and O.V. Karas. Computation of a Transonic Airfoil Flow Considering Viscous Effects and Thin Separated Regions. *Le Recherche Aerospatiale*, 1991(1):1–15, 1991.

[28] D. Kuchemann. Types of Flow on Swept Wings With Special Reference to Free Boundaries and Vortex Sheets. *Journal of the Royal Aeronautical Society*, 57:683–699, November 1953.

[29] H. Lamb. *Hydrodynamics.* Dover Publications, 1932.

[30] M. Lazareff and J.C. Le Balleur. Computation of Three-Dimensional Viscous Flow on Transonic Wings By Boundary-Layer Flow Interaction. *La Recherche Aerospatiale*, 3, 1983.

[31] J. T. Lee. *A Potential Based Panel Method for The Analysis of Marine Propellers in Steady Flow.* PhD thesis, Department of Ocean Engineering, Massachusetts Institute of Technology, August 1987.

[32] M. J. Lighthill. On Displacement Thickness. *Journal of Fluid Mechanics*, 4:383–392, 1958.

[33] R. C. Lock and B. R. Williams. Viscous-Inviscid Interactions in External Aerodynamics. *Progress in Aeronautical Sciences*, 24:51–171, 1987.

[34] E. A. Lurie. *Investigation of High Reduced Frequency, Separated Trailing Edge Flows.* PhD thesis, Department of Ocean Engineering, Massachusetts Institute of Technology, September 1996.

[35] W. B. Morgan and E. B. Caster. Prediction of the Aerodynamic Characteristics of Annular Airfoils. Technical Report 1830, DTMB, 1965.

[36] L. Morino and M. Gennaretti. Boundary Integral Equation Methods For Aerodynamics. In S. N. Atluri, editor, *Computational Nonlinear Mechanics in Aerospace Engineering*, volume 146, pages 279–315. AIAA Progress in Astronautics and Aeronautics, Washington, D.C., 1992.

[37] L. Morino and C.-C. Kuo. Subsonic Potential Aerodynamics For Complex Configurations: A General Theory. *AIAA Journal*, 12(2):191–197, February 1974.

[38] B. H. Mughal. A Calculation Method For The Three-Dimensional Boundary-Layer Equations in Integral Form. Master's thesis, Department of Aeronautics and Astronautics, Massachusetts Institute of Technology, September 1992.

[39] J. N. Newman. Distributions of Sources and Normal Dipoles Over a Quadrilateral Panel. *Journal of Engineering Mathematics*, 20:113–126, 1986.

[40] J. N. Newman. *Marine Hydrodynamics.* The MIT Press, Cambridge, Massachusetts, 1989.

[41] B. A. Nishida. *Fully Simultaneous Coupling of the Full Potential Equation and the Integral Boundary Layer Equations in Three Dimensions.* PhD thesis, Department of Aeronautics and Astronautics, Massachusetts Institute of Technology, February 1996.

[42] A. Oshima. Analysis of Three-Dimensional Boundary-Layer on Propeller Blade. In *Propellers/Shafting '94 Symposium*, Virginia Beach, VA, September 1994. SNAME.

[43] W. H. Press, S. A. Teukolsky, W. T. Vetterling, and B. P. Flannery. *Numerical Recipes in FORTRAN. The Art of Scientific Computing, 2nd Edition.* Cambridge University Press, New York, 1992.

[44] S. Pyo. *Numerical Modeling of Propeller Tip Flows with Wake Sheet Roll-up in Three Dimensions.* PhD thesis, Department of Ocean Engineering, Massachusetts Institute of Technology, September 1995.

[45] S. Pyo and S.A. Kinnas. The Flow Adapted Grid (FLAG) Applied to the Analysis of Propeller Tip Flows. In *Proceedings of the Propellers/Shafting '94 Symposium*, Virginia Beach, VA, September 1994. SNAME.

[46] W. D. Ramsey. *Boundary Integral Methods for Lifting Bodies with Vortex Wakes.* PhD thesis, Department of Ocean Engineering, Massachusetts Institute of Technology, May 1996.

[47] D. F. Rogers and J. A. Adams. *Mathematical Elements for Computer Graphics, 2nd Ed.* McGraw-Hill Book Co., 1990.

[48] J. W. Slooff. Technical Status Review on Drag Prediction and Analysis From Computational Fluid Dynamics: State of the Art. Technical Report AGARD-AR-256, AGARD, 1994. Forward and Conclusions.

[49] P. D. Smith. An Integral Prediction Method for Three-Dimensional Compressible Turbulent Boundary Layers. R & M 3739, Aeronautical Research Council, 1972.

[50] T. Swafford. Analytical Approximation of Two-Dimensional Separated Turbulent Boundary-Layer Velocity Profiles. *AIAA Journal*, 21(6):923–926, 1983.

[51] D. T. Valentine. Applicability of a Boundary-Integral Method to Marine Propulsor Problems. Technical Report CRDKNSWC/HD-1262-05, CDNSWC, October 1993.

[52] A. E. P. Veldman. A Numerical View on Strong Viscous-Inviscid Interaction. In W. G. Habashi, editor, *Computational Methods in Viscous Flows*, pages 343–363. Pineridge Press, Swansea, U. K., 1984.

[53] J. Wai and H. Yoshihara. Transonic Turbulent Separation on Swept Wings-A Return to the Direct Formulation. *AIAA-84-0265*, 1984.

[54] J. Weber, D. Kuchemann, and G.G. Brebner. Low-Speed Tests on 45-deg Swept-Back Wings Parts I and II. R & M 2882, Aeronautical Research Council, 1951.

[55] F. M. White. *Viscous Fluid Flow.* McGraw-Hill Book Co., 1991.

[56] L. Wigton and H. Yoshihara. Viscous-Inviscid Interactions With a Three-Dimensional Inverse Boundary Layer Code. In T. Cebeci, editor, *Numerical and Physical Aspects of Aerodynamic Flows II.* Springer - Verlag, January 1983.

Appendix A

Surface Representation by B-Splines

B-splines provide a simple, but very powerful, means of representing complex surfaces mathematically. This appendix provides a brief overview of tensor product B-spline surfaces and the transformation between derivatives in the B-spline parameter space and 3D Cartesian coordinates. The reader is directed to the book by Rogers and Adams [47] for a detailed treatment on B-splines.

A.1 Tensor Product B-spline Surfaces

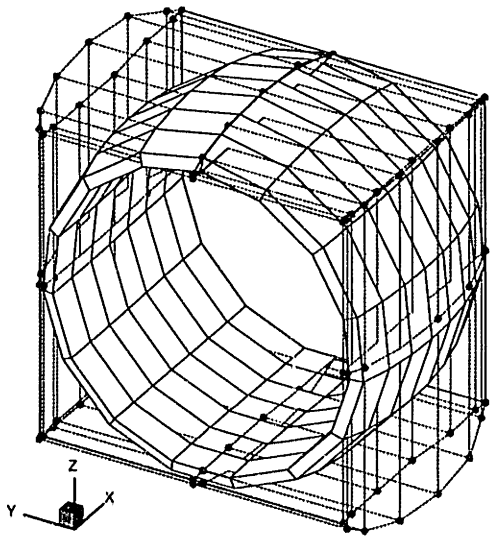

Figure A-1: B-spline surface with its control net. The vertices of the control net are shown as closed circles

A point **X** on the surface **S** shown in Figure A-1 is mapped from the point (s,t) in the parametric space by the tensor product B-spline expansion

$$\mathbf{X}(s,t) = \sum_{i=1}^{\bar{N}_s} \sum_{j=1}^{\bar{N}_t} \mathcal{X}_{i,j} S^{i,j}(s,t) \tag{A.1}$$

where $\mathcal{X}_{i,j}$ are known global Cartesian coordinates of the control net vertices, $S^{i,j}$ are the rational B-spline surface basis functions, and $\bar{N}_s$ and $\bar{N}_t$ are the number of control polygon vertices in the s and t directions respectively. The parameters s and t are assumed to be orthogonal to one another.

The rational B-spline surface basis functions are defined as

$$S^{i,j}(s,t) = \frac{h_{i,j}\mathcal{N}_{i,k}(s)\mathcal{M}_{j,l}(t)}{\sum_{i1=1}^{\bar{N}_s}\sum_{j1=1}^{\bar{N}_t} h_{i1,j1}\mathcal{N}_{i1,k}(s)\mathcal{M}_{j1,l}(t)} \tag{A.2}$$

where $\mathcal{N}_{i,k}(s)$ and $\mathcal{M}_{j,l}(t)$ are the normalized basis functions in the s and t directions respectively. $h_{i,j}$ are weights applied at each vertex which are assumed to be non-negative. Rational B-splines basis functions are used instead of the simpler, integral B-spline basis functions so conic sections can be represented exactly. If all the weights are set equal, integral B-spline basis functions are recovered.

The ith normalized basis function of order k^s, $\mathcal{N}_{i,k}(s)$, is defined using the Cox-deBoor recursion relations [47].

$$\mathcal{N}_{i,1}(s) = \begin{cases} 1 & \text{if } x_i \le s < x_{i+1} \\ 0 & \text{otherwise} \end{cases}$$

and

$$\mathcal{N}_{i,k}(s) = \frac{(s - x_i)N_{i,k-1}(s)}{x_{i+k-1} - x_i} + \frac{(x_{i+k} - s)N_{i+1,k-1}(s)}{x_{i+k} - x_i + 1} \tag{A.3}$$

where x_i is an element of the s direction knot vector. The basis function in the t direction, $\mathcal{M}_{j,l}(t)$, is defined in a similar manner.

A surface grid is generated by evaluating (A.1) at several values of the parameters s and t. Chordwise grid lines are evaluated with t fixed while spanwise grid lines are evaluated with s fixed.

A.2 Derivatives of the B-spline Expansion

We are ultimately interested in calculating the velocity tangent to the surface at point **X**. Surface tangent vectors can be evaluated analytically at any point on the

surface using the B-spline expansion. The tangent vectors are used to compute a transformation matrix relating derivatives in the parametric space to derivatives in the global system and to construct a local Cartesian coordinate system on the surface at $\mathbf{X}$.

The surface tangent vector in the s direction at point $\mathbf{X}$ is obtained by differentiating (A.1) with respect to s. $\mathbf{X}_s$ represents the differential change in each of the Cartesian coordinates along the surface due to a differential change of s at point $\mathbf{X}$.

$$\mathbf{X}_s = \frac{\partial \mathbf{X}}{\partial s} = (\frac{\partial X}{\partial s}, \frac{\partial Y}{\partial s}, \frac{\partial Z}{\partial s}) = \sum_{i=1}^{\bar{N}_s} \sum_{j=1}^{\bar{N}_t} \mathbf{X}_{i,j} S_s^{i,j}(s,t) \tag{A.4}$$

with $S_s^{i,j}(s,t)$ defined by

$$S_s = \frac{N}{D}\left(\frac{N_s}{N} - \frac{D_s}{D}\right) \tag{A.5}$$

N and D are the numerator and denominator of (A.2) with derivatives defined as

$$N_s = \sum_{i=1}^{\bar{N}_s} \sum_{1=1}^{\bar{N}_t} h_{i,j} B_{i,j} \mathcal{N}'_{i,k}(s) \mathcal{M}_{j,l}(t) \tag{A.6}$$

$$D_s = \sum_{i=1}^{\bar{N}_s} \sum_{1=1}^{\bar{N}_t} h_{i,j} \mathcal{N}'_{i,k}(s) \mathcal{M}_{j,l}(t) \tag{A.7}$$

The derivatives of the normalized basis function, $\mathcal{N}'$, are obtained by differentiating the Cox-deBoor recursion equations with respect to the parameter s. The tangent vector in the t direction, $\mathbf{X}_t$, is calculated in an analogous manner.

Introducing a third coordinate n, we define the outward unit normal vector at point $\mathbf{X}$ by

$$\hat{e}_n = \frac{\partial \mathbf{X}}{\partial n} = \frac{\frac{\partial \mathbf{X}}{\partial s} \times \frac{\partial \mathbf{X}}{\partial t}}{\left| \frac{\partial \mathbf{X}}{\partial s} \times \frac{\partial \mathbf{X}}{\partial t} \right|} \tag{A.8}$$

A.2.1 Calculation of the Transformation Matrix

$\mathbf{X}_s$, $\mathbf{X}_t$, and $\mathbf{X}_n$ are the columns of a transformation matrix which relates differential changes in global Cartesian coordinates to differential changes in the B-spline parametric coordinates at the point $\mathbf{X}$.

$$\begin{Bmatrix} dX \\ dY \\ dZ \end{Bmatrix} = \begin{bmatrix} \frac{\partial X}{\partial s} & \frac{\partial X}{\partial t} & \frac{\partial X}{\partial n} \\ \frac{\partial Y}{\partial s} & \frac{\partial Y}{\partial t} & \frac{\partial Y}{\partial n} \\ \frac{\partial Z}{\partial s} & \frac{\partial Z}{\partial t} & \frac{\partial Z}{\partial n} \end{bmatrix} \begin{Bmatrix} ds \\ dt \\ dn \end{Bmatrix} \tag{A.9}$$

wake layer

$$\begin{aligned}
\Delta C_{\mathcal{D}} &= \int \tau_x \frac{\partial u}{\partial \eta} d\eta + \int \tau_z \frac{\partial w}{\partial \eta} d\eta \\
&= \int \tau_x \frac{\partial u}{\partial \eta} d\eta + \int \tau_z \frac{\partial w}{\partial \eta} d\eta \\
&= \left(\int \tau_x \frac{\partial u}{\partial \eta} d\eta \right) \left(1.0 + A_c^2 \right) \\
&= C_\tau (1.0 - U_s)(1.0 + A_c^2)
\end{aligned} \tag{B.23}$$

The total dissipation coefficient is given by $C_{\mathcal{D}} = C_{\mathcal{D}w} + \Delta C_{\mathcal{D}}$

Appendix C

Velocity and Displacement Thickness Sensitivities

The coupling between the inner and outer flows is introduced through the edge velocity equations. The sensitivity formulae relating the edge velocities and displacement thicknesses to the streamwise-crossflow components of mass defect are derived in this section. The equations presented here extend the sensitivity formulae used by Drela [10] in two dimensions to three dimensions.

The velocity sensitivities are formed by combining the elements of the velocity-mass defect influence coefficient matrices that were presented in Chapter 4. Since they depend on the direction of outer flow streamlines which is determined as part of the coupled boundary-layer/potential flow solution, the sensitivities must be recomputed for each Newton iteration

C.1 Edge Velocity Sensitivities

(4.18) and (4.19) define the edge velocities as functions of mass defect in the surface coordinate system that wraps around the wing (see Figure 2-3). (4.18) is restated here for convenience. At node i, the chordwise component of edge velocity is

$$u_{ei} = u_{ei}^{(I)} + \sum_{k=1}^{N_{nodes}} E_{ik}^{x}(m_x)_k + \sum_{k=1}^{N_{nodes}} F_{ik}^{x}(m_z)_k \tag{C.1}$$

where E^x and F^x are the influence coefficients defined in §4.3.2, $u_{ei}^{(I)}$ is the base inviscid velocity tangent to the surface, and m_x and m_z are the components of mass defect in the surface coordinate system. The base inviscid velocity includes the free stream and inviscid perturbation velocity and is written as a single term to simplify notation. The

x-z components of mass defect are replaced with streamwise-crossflow *1-2* components of mass defect by substituting the 2D rotational transformation equations into the edge velocity equation.

$$\begin{aligned} m_x &= m_1 \cos\alpha - m_2 \sin\alpha \\ m_z &= m_1 \sin\alpha + m_2 \cos\alpha \end{aligned} \tag{C.2}$$

where $\cos\alpha \equiv \frac{u_e}{q_e}$ and $\sin\alpha \equiv \frac{w_e}{q_e}$. The chordwise edge velocity, expressed as a function of streamwise-crossflow mass defect, is:

$$\begin{aligned} u_{ei} = u_{ei}^{(I)} &+ \sum_{k=1}^{N_{nodes}} \left(E_{ik}^x \cos\alpha + F_{ik}^x \sin\alpha\right)(m_1)_k \\ &+ \sum_{k=1}^{N_{nodes}} \left(-E_{ik}^x \sin\alpha + F_{ik}^x \cos\alpha\right)(m_2)_k \end{aligned} \tag{C.3}$$

The components of the rotational transformation matrix, $\cos\alpha$ and $\sin\alpha$, are calculated at the k^{th} node using the local edge velocity from the previous iteration. Finally, the sensitivities are derived by differentiating (C.3) with respect to m_1 and m_2.

$$\frac{\partial u_{ei}}{\partial m_{1k}} = \left(E_{ik}^x \cos\alpha + F_{ik}^x \sin\alpha\right) \tag{C.4}$$

$$\frac{\partial u_{ei}}{\partial m_{2k}} = \left(-E_{ik}^x \sin\alpha + F_{ik}^x \cos\alpha\right) \tag{C.5}$$

The sensitivities for the spanwise velocities are derived from (4.19) in a similar manner.

$$\frac{\partial w_{ei}}{\partial m_{1k}} = \left(E_{ik}^z \cos\alpha + F_{ik}^z \sin\alpha\right) \tag{C.6}$$

$$\frac{\partial w_{ei}}{\partial m_{2k}} = \left(-E_{ik}^z \sin\alpha + F_{ik}^z \cos\alpha\right) \tag{C.7}$$

These equations define the sensitivity of the edge velocities at node i to the streamwise-crossflow components of mass defect at node k.

C.2 Displacement Thickness Sensitivities

The streamwise component of displacement thickness is

$$\delta_1^* \equiv \frac{m_1}{q_e} \tag{C.8}$$

where q_e is the magnitude of the edge velocity

$$q_e = \sqrt{u_e^2 + w_e^2} \tag{C.9}$$

The sensitivity formulae for $\frac{\partial \delta_1^*}{\partial m_1}$ and $\frac{\partial \delta_1^*}{\partial m_2}$ are derived by differentiating (C.8) by chain rule, with the understanding that q_e is also a function of the mass defect.

$$\frac{\partial \delta_1^*}{\partial m_1} = \frac{1}{q_e} - \frac{m_1}{q_e^2}\frac{\partial q_e}{\partial m_1} \tag{C.10}$$

with

$$\frac{\partial q_e}{\partial m_1} = \frac{\partial q_e}{\partial u_e}\frac{\partial u_e}{\partial m_1} + \frac{\partial q_e}{\partial w_e}\frac{\partial w_e}{\partial m_1} \tag{C.11}$$

The discrete sensitivity formulae for the streamwise displacement thickness are obtained by inserting the edge velocity-mass defect sensitivities from the previous section into (C.10). At node i,

$$\frac{\partial \delta_{1i}^*}{\partial m_{1k}} = \left[-\frac{m_1}{q_e^2}\left(\frac{\partial q_e}{\partial u_e}\frac{\partial u_{ei}}{\partial m_{1k}} + \frac{\partial q_e}{\partial w_e}\frac{\partial w_{ei}}{\partial m_{1k}}\right)\right] + \frac{\delta_{ik}}{q_e} \tag{C.12}$$

$$\frac{\partial \delta_{1i}^*}{\partial m_{2k}} = \left[-\frac{m_1}{q_e^2}\left(\frac{\partial q_e}{\partial u_e}\frac{\partial u_{ei}}{\partial m_{2k}} + \frac{\partial q_e}{\partial w_e}\frac{\partial w_{ei}}{\partial m_{2k}}\right)\right] \tag{C.13}$$

The equations are evaluated using the current values of q_e, m_1, m_2, $\frac{\partial q_e}{\partial u_e}$, and $\frac{\partial q_e}{\partial w_e}$ at node i. The last term in (C.12) is non-zero only when $i = k$.

The equivalent sensitivities for the crossflow component of displacement thickness are:

$$\frac{\partial \delta_{2i}^*}{\partial m_{1k}} = \left[-\frac{m_1}{q_e^2}\left(\frac{\partial q_e}{\partial u_e}\frac{\partial u_{ei}}{\partial m_{1k}} + \frac{\partial q_e}{\partial w_e}\frac{\partial w_{ei}}{\partial m_{1k}}\right)\right] \tag{C.14}$$

$$\frac{\partial \delta_{2i}^*}{\partial m_{2k}} = \left[-\frac{m_1}{q_e^2}\left(\frac{\partial q_e}{\partial u_e}\frac{\partial u_{ei}}{\partial m_{2k}} + \frac{\partial q_e}{\partial w_e}\frac{\partial w_{ei}}{\partial m_{2k}}\right)\right] + \frac{\delta_{ik}}{q_e} \tag{C.15}$$